Zircon-hosted melt inclusion record of silicic magmatism in the Mesoproterozoic St. Francois Mountains terrane, Missouri: Origin of the Pea Ridge iron oxide-apatite-rare earth element deposit and implications for regional crustal pathways of mineralization

Kathryn E. Watts [a,*], Celestine N. Mercer [b]

[a] *U.S. Geological Survey, 350 North Akron Road, Moffett Field, CA, United States*
[b] *U.S. Geological Survey, Denver Federal Center, Lakewood, CO, United States*

Abstract

Voluminous silicic magmatism was coeval with iron ore mineralization in the St. Francois Mountains terrane in southeast Missouri, part of the broader Mesoproterozoic Granite-Rhyolite province along the eastern margin of Laurentia. Some of the iron deposits contain extraordinary endowments of critical elements, such as the Pea Ridge iron oxide-apatite (IOA) deposit, which has an average grade of ∼12 wt% rare earth oxides in breccia pipes that flank the ore body. To assess the role of silicic magmatism in the genesis of the Pea Ridge deposit, we present a high-spatial resolution study of zircon-hosted melt inclusions from rhyolitic ash-flow tuffs. Melt inclusion data are combined with textural, geochemical, and geochronological analyses of zircon hosts to elucidate the magmatic-hydrothermal evolution of the Pea Ridge system. Two contemporaneous silicic igneous centers in the St. Francois Mountains terrane, Bourbon and Eminence, were studied for comparison. Pea Ridge melt inclusions are trachydacitic to rhyolitic (∼63–79 wt% SiO_2, ∼5.6–11.7 wt% $Na_2O + K_2O$) with very high Cl in the least-evolved and most alkaline melt inclusions (∼2000–5000 ppm Cl). Rare earth elements (REE) in melt inclusions have identical chondrite-normalized patterns to the mineralized breccia pipes, but with systematically lower absolute concentrations. Haplogranite ternary pressures range from ∼0.5 to 10 kbar, with an average of ∼2–3 kbar (7–12 km depth), and liquidus temperatures are ∼850–950 °C, with an average of ∼920 °C. Silicate and phosphate mineral inclusions have compositions that overlap minerals from the iron ore body and breccia pipes, recording a transition from igneous to hydrothermal zircon growth. Igneous iron oxide inclusions have compositions that indicate Pea Ridge magmas were reduced to moderately oxidized (log fO_2 of −0.8 to −1.84 ΔNNO). Zircons from two Pea Ridge samples have $^{207}Pb/^{206}Pb$ concordia ages of 1456 ± 9 Ma and 1467 ± 13 Ma that overlap published ages for the breccia pipes and iron ore zones of the Pea Ridge deposit. A population of texturally and chemically disrupted zircons have discordant domains that correspond to high Fe, U, and REE concentrations, consistent with the unique geochemical attributes of the IOA-REE ore body. Inherited cores in Pea Ridge and Bourbon zircons have concordant $^{207}Pb/^{206}Pb$ dates of 1550–1618 Ma, providing direct evidence of cratonic basement beneath these centers. Oxygen isotope data for inherited and autocrystic igneous zircons span from mantle to crustal values ($\delta^{18}O_{zircon}$ = 5.5–7.9‰). Our data are consistent with a model in which metasomatized mantle components were mixed with cratonic and accreted crustal material in a back-arc or rifted segment of a volcanic arc, with ore fluids derived from Cl-rich melts to transport Fe and REE in a long-lived (tens of Myr), pulsed, magmatic-hydrothermal system. Bourbon, which also possesses IOA mineralization, shares key petrologic similarities with the Pea Ridge system, whereas Eminence, which is

* Corresponding author.
E-mail address: kwatts@usgs.gov (K.E. Watts).

not mineralized, has disparate geochemical and isotopic signatures that indicate it formed in a different crustal setting. The location of Pea Ridge and Bourbon along a cratonic margin may have been important in focusing silicic melts and mineralization in the upper crust, serving as a guide for future exploration efforts.

1. INTRODUCTION

Globally, there exists an economically important class of iron-rich deposits that include iron oxide-copper-gold (IOCG), for which the type locality is Olympic Dam in southern Australia, and iron oxide-apatite (IOA), for which the type locality is Kiruna in northern Sweden (Hitzman et al., 1992). These deposit types vary in detail, but are broadly similar in that they contain massive bodies of Ti-poor iron oxides, are often hosted in volcanic and intrusive intermediate to felsic rocks, have large breccia zones along their margins, and pervasive sodic-potassic alteration that can extend to regional scales (see reviews by Hitzman et al., 1992; Williams et al., 2005; Groves et al., 2010; Barton, 2014). IOCG deposits have economic Cu and Au grades, and both IOCG and IOA deposits may contain elevated concentrations of other economically important elements, such as the rare earth elements (REE) (e.g., Oreskes and Einaudi, 1990; Nuelle et al., 1992). Because they are essential to modern technology but with limited global supply, the REE have been designated as "critical" and research interest in their origins has risen sharply in recent years (Verplanck and Hitzman, 2016).

Considerable debate persists as to the linkages between IOCG and IOA deposits and their ore-forming conditions. For example, ore-forming fluids for IOCG and IOA deposits have been hypothesized to have igneous origins (either an immiscible melt or aqueous fluid exsolved from magma), metamorphic origins (possibly related to collisional tectonics along active continental margins), terrestrial-hydrothermal origins (derived from surficial basins as meteoric waters or brines), or a combination thereof (see review by Barton, 2014). While some of the largest IOCG and IOA deposits are Precambrian in age, there are numerous deposits with ages that extend into the Cenozoic, and they occur on every continent (Williams et al., 2005). The geologic and tectonic associations of the deposits are likewise diverse, but many of the Precambrian examples are found along the margins of cratons and may be linked to supercontinent assembly and breakup cycles and influx of mantle-derived magmas into the lithosphere. Metasomatism during prior subduction events may have enriched regions of the lithosphere in the metals and volatiles characteristic of IOCG and IOA deposits (Groves et al., 2010).

In localities where both IOCG and IOA deposits occur together, such as in the Jurassic–Cretaceous Chilean iron belt, there is a systematic relationship with depth and deposit type, with IOCG (hematite-dominant) ore zones occurring at shallower crustal levels and IOA (magnetite- and apatite-dominant) ore zones at deeper levels (Sillitoe, 2003; cf. Barra et al., 2017). Contrasting models have been invoked to explain these deposits. A magnetite flotation model posits that igneous magnetite microlites serve as wetting sites for exsolved aqueous fluids that scavenge Fe, P, S, Cu and Au from the magma, followed by buoyant ascension, cooling and precipitation of hydrothermal magnetite and apatite (forming a lower IOA ore zone), and then as the ore fluids continue to ascend and oxidize, magnetite, hematite and Fe-Cu-Au sulfides precipitate (forming an upper IOCG ore zone) (e.g., Knipping et al., 2015a, b; Simon et al., 2018; Ovalle et al., 2018; Knipping et al., 2019). Other models advocate formation of iron ore bodies from direct crystallization of geochemically unusual Fe-rich melts (e.g., Velasco et al., 2016; Tornos et al., 2016, 2017; Mungall et al., 2018; Xie et al., 2019) or by hydrothermal replacement of igneous host rocks by Fe-rich fluids with ligand contributions from magmatic and crustal sources (e.g., Dare et al., 2015). In the purely non-magmatic end member, magmas may not supply any of the constituent elements, but simply a heat source for leaching of these elements by saline brines in the shallow crust (e.g., Barton, 2014).

The focus of this study is on spatially and temporally linked IOCG and IOA deposits in the southeast Missouri iron metallogenic province in the St. Francois Mountains terrane (Kisvarsanyi and Proctor, 1967; Nold et al., 2014; Day et al., 2016). One of the largest IOA deposits in the region is Pea Ridge, which has an estimated iron ore resource (mined plus reserves) of >200 million metric tons (Mt), with an average grade of 53–55 wt% Fe for mined ore (Slack et al., 2016). As a whole, the region has an estimated iron ore resource of about 1000 Mt, which is within a factor of ~2–3 of world-class deposits at Olympic Dam and Kiruna (Williams et al., 2005). Like Olympic Dam and Kiruna, IOCG and IOA deposits in the St. Francois Mountains terrane occur along a craton margin and formed during the late Precambrian. Importantly, like the Chilean iron belt, there appears to be a continuum, or evolution in which IOA deposits form at deeper levels of the crust and transition into IOCG deposits at shallower levels (Day et al., 2016). The St. Francois Mountains terrane may therefore be a critical location to investigate potential genetic connections between IOCG and IOA deposits. In addition, Pea Ridge is associated with extremely high concentrations of REE in breccia pipes that cross-cut the IOA deposit, which have an average grade of ~12 wt% rare earth oxides (Seeger, 2000). Though the tonnage of known REE-rich breccia pipes is moderate (~200,000 tons), it is an important locality for understanding the geologic factors that produce anomalous concentrations of critical elements in IOA systems.

The purpose of this study is to provide a high-resolution petrologic study of the igneous host rocks of the Pea Ridge deposit, and several other broadly coeval igneous centers (Bourbon, Eminence) in the St. Francois Mountains terrane. Due to the antiquity and widespread alteration of the rocks, refractory zircon crystals were used to constrain primary igneous conditions and identify the intensive parameters underpinning local and region centers of magmatism and mineralization. Combining geochemical data for melt and mineral inclusions in zircon, with geochemical, isotopic, and geochronologic data for zircon hosts, this study provides an unprecedented view into the evolution of long-lived magmatic-hydrothermal systems that have produced IOA deposits. Specific contributions of this work include: (1) determining elemental endowments of primary magmas based on analyses of melt inclusions, (2) providing temperature, pressure and oxygen fugacity constraints for host igneous systems, (3) tracking the evolution of igneous to hydrothermal conditions of zircon growth, (4) establishing $^{207}Pb/^{206}Pb$ zircon crystallization ages for igneous units, and (5) identifying differences in crustal and mantle sources for mineralized (Pea Ridge, Bourbon) versus barren (Eminence) magmatic centers. Each of these factors are important for testing and refining ore deposit models and identifying prospective regions for IOCG and IOA-(REE) deposits.

2. GEOLOGIC BACKGROUND

2.1. Regional geology

Exposures of Mesoproterozoic rocks in the St. Francois Mountains, and analogous basement rocks beneath Cambrian and younger sedimentary cover in southeastern Missouri, delineate the St. Francois Mountains terrane (Fig. 1a). It comprises Mesoproterozoic (1.50–1.44 Ga) caldera-forming rhyolitic tuffs and intrusions and middle Mesoproterozoic (1.33–1.30 Ga) granitic intrusions, which form part of the Granite-Rhyolite province in North America (Fig. 1b, Kisvarsanyi, 1981; Van Schmus et al., 1996; Mengue et al., 2002; Bickford et al., 2015; Day et al., 2016). The Granite-Rhyolite province lies between the older Mazatzal (1.7–1.6 Ga) province to the west and the younger Grenville (1.3–0.9 Ga) province to the east, which formed in succession along the eastern margin of Laurentia during an ∼800 Myr period of accretionary orogenesis (Fig. 1b and c, Whitmeyer and Karlstrom, 2007). Age and isotopic data have been used to differentiate a cratonal origin of rhyolites to the northwest (>1.6 Ga) and a more juvenile origin to the southeast (<1.6 Ga), with the boundary at about 1.55 Ga along the western margin of the St. Francois Mountains terrane and the Granite-Rhyolite province (Fig. 1b, Bickford et al., 2015). Whereas the Mazatzal and Granite-Rhyolite provinces formed during the assembly (Mazatzal) and then breakup (Granite-Rhyolite) of supercontinent Columbia (Fig. 1c), the Grenville province formed during the assembly of supercontinent Rodinia (Whitmeyer and Karlstrom, 2007).

Accretionary growth of Laurentia along a long-lived convergent margin involved complex tectonic processes that are difficult to discern in Mesoproterozoic rocks. The lack of metamorphism in the St. Francois Mountains terrane has been used as evidence against compression during its inception, and some workers advocate extension, perhaps in a back-arc setting along an active or recently active subduction zone (e.g., Mengue et al., 2002). Extension in a back-arc setting would have facilitated mantle decompression and melting, which may have been aided by other processes such as slab break off or roll back (Bickford et al., 2015). Intermediate calc-alkaline rocks from a juvenile arc are hypothetical protoliths for silicic magmas of the St. Francois Mountains terrane (Mengue et al., 2002; Ayuso et al., 2016). Accretion of metasomatized arc rocks to the continental margin as the locus of subduction shifted southeastward is consistent with tectonic models (Whitmeyer and Karlstrom, 2007). Cratonic (>1.55 Ga) crust bounds the western margin of the St. Francois Mountains terrane (Fig. 1a and b, Bickford et al., 2015), and this boundary may have served to focus heat and melting of metasomatized rocks and provided a pathway for magmas, fluids, and metals in generating the region's prodigious igneous rocks and iron ore bodies (e.g., Ayuso et al., 2016).

Iron mineralization in the southeast Missouri iron metallogenic province is diverse and extensive, with >20 iron deposits that span the St. Francois Mountains terrane (most significant deposits shown in Fig. 1a), and several newly identified prospective areas based on combined aeromagnetic and gravity gradiometry data (McCafferty et al., 2016). Host rocks are typically rhyolitic volcanics, and geochronologic data indicate that silicic magmatism and mineralization occurred during the early Mesoproterzoic (1.50–1.44 Ga) phase of igneous activity in the St. Francois Mountains terrane (Van Schmus et al., 1996; Aleinikoff et al., 2016; Neymark et al., 2016). In addition to IOA and IOCG deposits, there are hydrothermal iron oxide veins, sedimentary exhalative iron deposits, and iron-rich skarns (Nold et al., 2014; Day et al., 2016). IOA deposits are the most abundant, with significant iron ore production at Pea Ridge (>50 Mt), Pilot Knob (∼20 Mt), and Iron Mountain (∼9 Mt) (Nold et al., 2014; Day et al., 2016). Other less well-characterized IOA deposits include Kratz Spring, Bourbon, and Camels Hump (Seeger, 2000, 2003; Day et al., 2016). Although not developed, Boss is the most significant IOCG deposit, with a drill-indicated reserve of ∼40 Mt at 0.8 wt% Cu, the highest known base metal content in the region (Day et al., 2001). Reconstruction of the Mesoproterozoic crustal profile based on drill cores and surface exposures indicate vertical zonation in deposit type and mineralogy, with high-temperature, magnetite-rich IOA deposits emplaced at depths of ∼1–2 km and low-temperature, hematite-rich IOCG deposits emplaced at subvolcanic depths (<1 km), capped by near-surface epithermal and sedimentary exhalative deposits (Day et al., 2016; Hofstra et al., 2016).

2.2. Local geology for sites in this study

2.2.1. Pea ridge

Pea Ridge is located in the northern St. Francois Mountains terrane, about 14 km southeast of the town of Sullivan
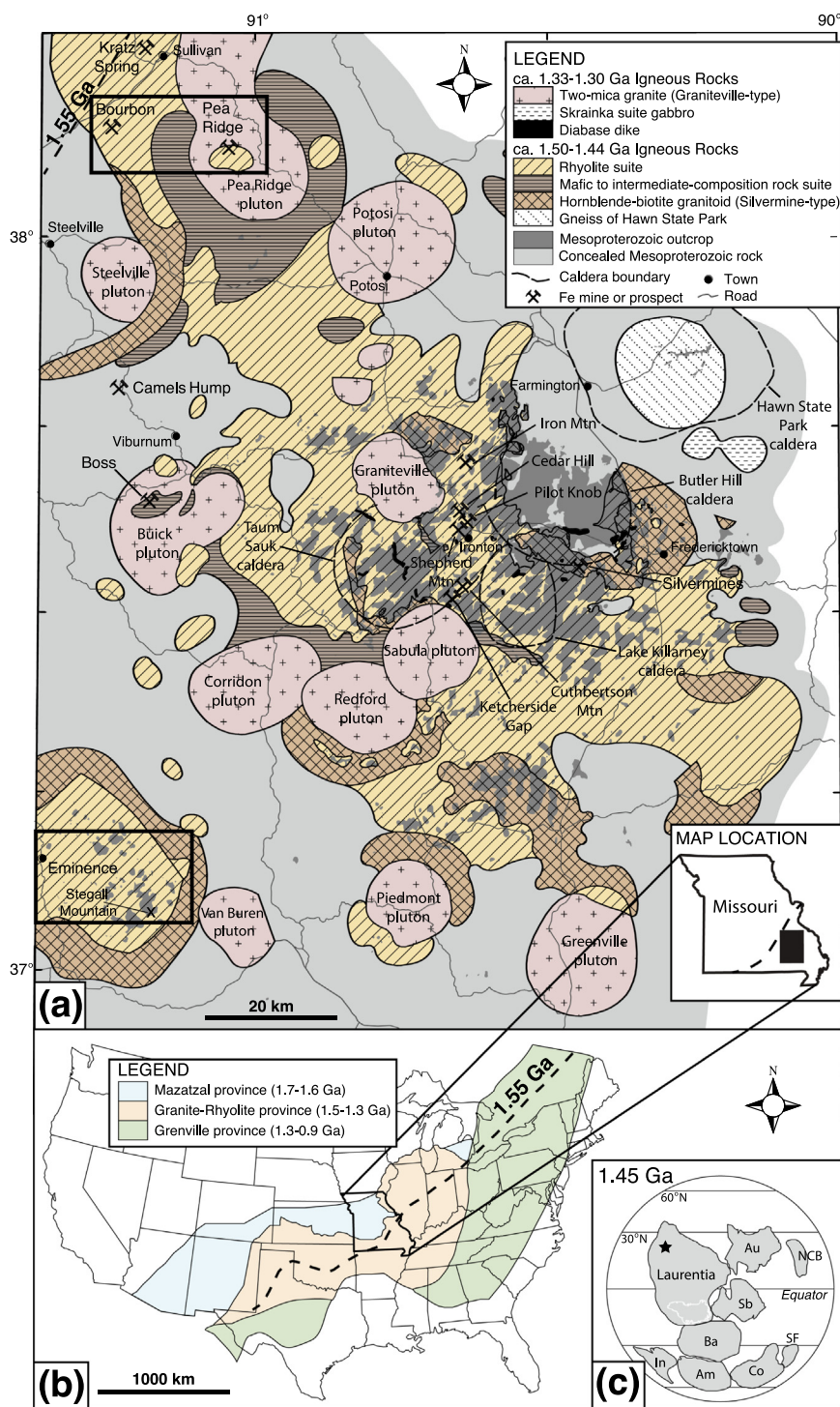
Fig. 1. (a) Simplified geologic map of the St. Francois Mountains terrane. Mesoproterozoic outcrops are shown in the dark gray shading, and patterned polygons show the types, ages, and distributions of igneous rocks based on surface exposures and drill cores. Light gray shading in the background shows the inferred extent of concealed Mesoproterozoic basement rocks. Bold outlined boxes show the regions included in this study: Pea Ridge, Bourbon, and Eminence. Inset at the bottom shows the map location in southeast Missouri, with the solid black box showing the map area. The location of the 1.55 Ga basement isopleth is shown by the bold dashed line. (b) Map of the United States showing the location of the St. Francois Mountains terrane in the Granite-Rhyolite province, bounded by the Mazatzal province to the west and Grenville province to the east. The location of the 1.55 Ga basement isopleth is shown by the bold dashed line. (c) Global configuration of supercontinent Columbia at 1.45 Ga. Laurentia is labeled, with a white outline of Greenland for scale and orientation. Au = Australia, Sb = Siberia Ba = Baltica, Am = Amazonia, In = India, Co = Congo, SF = Sao Francisco, NCB = North China Block. The black star shows the approximate location of the St. Francois Mountains terrane in Laurentia at 1.45 Ga. Compiled from and adapted after Pratt et al. (1979), Kisvarsanyi (1981), Van Schmus et al. (1996), Bickford et al. (2015), Day et al. (2016), and Meert and Santosh (2017).

(Fig. 1). It was Missouri's most economically important iron deposit, mined from 1964 to 2001. The tabular Pea Ridge IOA ore body strikes ca. N 60°E and dips steeply to the southeast, cross-cutting a sequence of rhyolitic ash-flow tuff units that strike ca. N 80°W and dip steeply northeast (Day et al., 2016). The deposit and host ash-flow tuffs are concealed by ~400 m of Paleozoic sedimentary rocks (Day et al., 2016). The paragenetic sequence of alteration zones in the IOA deposit, from oldest to youngest, includes an amphibole-quartz zone, massive magnetite zone, magnetite- and hematite-cemented breccias, specular hematite, a silicified zone, and REE-bearing breccia pipes (Nuelle et al., 1992; Seeger et al., 2001; Day et al., 2016). Rhyolitic wall rocks exhibit partial to total replacement by Fe-oxides, with roundness and level of alteration of wall rock fragments increasing towards the ore body (Nuelle et al., 1992). Four breccia pipes exposed at a depth of ~700 m along the eastern margin of the deposit contain an extraordinary endowment of rare earth oxides (~4–38 wt%) (Seeger, 2000, 2003). Published zircon U-Pb dates on two of the host ash-flow tuff units are 1474 ± 8 and 1473 ± 6 Ma (Aleinikoff et al., 2016). Ore mineralization ages are constrained by apatite and monazite from the amphibole-quartz and magnetite ore zones (Neymark et al., 2016) and monazite and xenotime from the REE-bearing breccia pipes (Aleinikoff et al., 2016); these dates indicate that there were multiple superimposed metasomatic events from ~1470–1440 Ma that were within error of host rhyolites to ~30 Myr younger. Aleinikoff et al. (2016) interpret a clustering of monazite and xenotime dates at ~1465 Ma as indicative of the formation age of the REE-bearing breccia pipes.

2.2.2. Bourbon

Bourbon is ~18 km west of Pea Ridge and concealed by a comparable thickness (~450 m) of Paleozoic sedimentary cover (Fig. 1a, McMillan, 1946; Seeger, 2003). Drill core records from the 1940s document a >250 m section of rhyolite porphyry that hosts the deposit (Cullison and Ellison, 1944; McMillan, 1946, Damon, 1949). Rhyolitic host rocks have zircon U-Pb dates of 1472–1463 ± 11–12 Ma (Aleinikoff, unpublished data), within uncertainty of host rhyolites at Pea Ridge (Aleinikoff et al., 2016). Like Pea Ridge, mineralization at Bourbon is dominated by massive magnetite with iron oxide-cemented breccias along its margins (Seeger, 2003). It has a mineralogy characteristic of IOA deposits. Bourbon has the largest geophysical footprint (~13 km²) of iron deposits in the St. Francois Mountains terrane, based on combined magnetic and gravity anomaly data (McCafferty et al., 2016). Bourbon's footprint is similar to that of Boss (~11 km²), the region's most significant IOCG deposit, and much larger than that of Pea Ridge (~4 km²), which has had the most production (McCafferty et al., 2016). It may therefore be an attractive target for future exploration efforts.

2.2.3. Eminence

Eminence is ~110 km south of Pea Ridge and Bourbon, along the far southwestern edge of the St. Francois Mountains terrane (Fig. 1). Outcrops of volcanic Meso-

proterozoic rocks are present at Stegall Mountain and other hills and knobs north and west, surrounded by thick deposits (up to ~300 m) of Paleozoic sedimentary rocks (Orndorff et al., 1999; Harrison et al., 2002). Kisvarsanyi (1981) first hypothesized that Eminence was the site of a large caldera system based on the presence of voluminous rhyolitic ash-flow tuffs, lavas and megabreccia deposits, and drill core intercepts of granodiorite and syenite along its perimeter. The lower sequence of volcanic rocks is dominated by rhyolitic ash-flow tuffs with steeply dipping foliations that are interpreted to represent rotation during caldera collapse, whereas the upper sequence is marked by deposition of a subhorizontal air-fall tuff unit that post-dated caldera collapse and voluminous post-caldera lava flows and domes (Harrison et al., 2002). A zircon U-Pb date of 1470 ± 3 Ma was obtained for one of the upper sequence rhyolites (rhyolite of Shut-In Mountain) (Harrison et al., 2000). Additional zircon U-Pb dates for lower and upper sequence volcanic rocks span from 1467 to 1462 ± 5–7 Ma (Aleinikoff, unpublished data). There are no known iron deposits at Eminence, and regional aeromagnetic and gravity maps do not reveal any anomalies that would indicate iron deposits at depth (McCafferty et al., 2019).

3. SAMPLES AND METHODS

3.1. Samples

3.1.1. Pea ridge

Rhyolitic ash-flow tuff units have been informally referred to as "porphyries" with a numerical nomenclature that corresponds to the mine level depth (in feet) with the best exposures of individual units (see Seeger et al., 2001; Day et al., 2016). Sample PR-91 is part of the 2275 porphyry unit, a red tuff with quartz, plagioclase, and alkali feldspar that overlies the 1975 porphyry and an unnamed tuff unit. Sample PR-12 is part of the black porphyry unit (no numerical prefix), a crystal-rich tuff with quartz, alkali feldspar, plagioclase, and hornblende. It is discontinuous between the 1825 porphyry and 1675 porphyry that lie stratigraphically above the 2275 porphyry.

3.1.2. Bourbon

Sample Bourb-204 is a trachydacite unit that lies stratigraphically beneath a rhyolite unit that hosts iron ore. It was collected from drill hole B-24 at a depth interval of 2310–2329 feet. It contains plagioclase, alkali feldspar, quartz, clinopyroxene, and hornblende. We note that though host rocks to the Bourbon IOA deposit have generally been described as "rhyolite porphyry," they are variable and trend towards intermediate (andesite to trachyandesite) compositions (du Bray et al., 2018). Bourb-204 may be part of an intermediate ring-fracture intrusion projected along the western margin of the Pea Ridge caldera.

3.1.3. Eminence

Eminence samples include the lower (MO14-009) and upper (MO14-007) unit of Coot Mountain rhyolite (units

Ycl and Ycu of Orndorff et al., 1999) and the rhyolite of Stegall Mountain (MO14-003, unit Ysm of Harrison et al., 2002). Whereas the lower and upper units of Coot Mountain rhyolite are the stratigraphically lowest rocks in the lower sequence of volcanic rocks at Eminence (Orndorff et al., 1999; Lowell et al., 2010), the rhyolite of Stegall Mountain belongs to the upper sequence (Harrison et al., 2002). Samples contain quartz, alkali feldspar, and plagioclase. Harrison et al. (2002) interpreted the rhyolite of Stegall Mountain to be a less quartz-rich variant of the rhyolite of Shut-In Mountain, one of the most voluminous lavas in the region with a thickness of >250 m.

3.2. Methods

3.2.1. Sample preparation

Zircons for each sample were obtained from J. Aleinikoff and Pea Ridge samples correspond to those published in Aleinikoff et al. (2016). The zircons were separated from whole rocks by standard methods including crushing, Frantz magnetic processing, and density concentration by methylene iodide. A few zircon samples were further processed to remove pyrite with a 7 N nitric (HNO_3) acid bath in a Pyrex beaker, heated on a hotplate until all pyrite was dissolved, and then rinsed six times with deionized water. Aliquots of zircon separates for each sample were processed in T. Sisson's experimental petrology laboratory at the U.S. Geological Survey (USGS) in Menlo Park, California. Melt inclusion homogenization methods were modified from Mercer et al. (2015). Bulk zircon aliquots (3–7 mg per sample) were loaded into gold capsules that were loosely crimped closed and placed in a ZHM (zirconium-hafnium-molybdenum) cold-seal pressure vessel with a pressure medium of pure Ar gas. The pressure vessel was placed vertically in a Deltech DT31VT resistance furnace and held at approximately 140 MPa, using a Heise gauge to maintain pressures to ±3 MPa, and heated to a temperature of 1000 °C, maintained to ±7 °C with a Pt-Pt$_{90}$-Rh$_{10}$ thermocouple in the ZHM pressure vessel. Experiments were held at target pressure and temperature conditions for 40 minutes and then rapidly (≥200 °C/s) quenched by inverting the pressure vessel and allowing the capsule to fall against the water-cooled pressure seal.

Zircons were bulk-mounted in 1-inch diameter round epoxy discs, including homogenized and non-homogenized aliquots, with standards for zircon and melt inclusion glass analyses (described in Section 3.2.3.). Zircons and standards were mounted within a 10 mm diameter in the center of each mount. A thin layer of superglue was spread across the upper surface of each mount using a metal needle, which served to fill interstitial spaces between grains and prevent plucking during polishing. Discs were ground down using a series of grits and polishing laps until bulk zircons were exposed to their approximate midsections, maximizing the number of exposed melt inclusions. This process was repeated multiple times for each mount, with multiple analytical sessions to collect data for each successive batch of exposed melt inclusions. Backscattered electrons (BSE) and cathodoluminescence (CL) imaging of the zircon mounts was performed with a Tescan VEGA3 scanning electron microscope at the USGS Menlo Park microanalytical facility, operated at 15–20 kV and 10–15 nA for BSE and 10 kV and 14–18 nA for CL. Energy dispersive spectra (EDS) were collected during BSE imaging sessions to identify different melt and mineral inclusion types within zircons.

3.2.2. Electron microprobe analyses

Silicate melt inclusions and mineral inclusions of quartz, alkali feldspar, and mica were analyzed with a JEOL 8900 electron microprobe at the USGS Menlo Park microanalytical facility (Supplementary Data Tables 1–2). The microprobe was operated at 15 kV and 5 nA with a 1–5 μm diameter beam. Additional silicate melt inclusions were analyzed with a JEOL JXA-8230 SuperProbe electron microprobe at the Stanford University Mineral and Microchemical Analysis Facility, using the same operating conditions and the same USGS glass and mineral standards to calibrate major and trace element geochemical analyses. Monazite and xenotime inclusions were analyzed with the JEOL 8900 electron microprobe in Menlo Park, operated at 20 kV and 30 nA with a 1 μm beam (Supplementary Data Table 3). Synthetic phosphate standards were used to calibrate REE analyses, with average detection limits of ~100–200 ppm for REE. Magnetite and ilmenite inclusions were analyzed with the JEOL JXA-8230 SuperProbe at Stanford, operated at 20 kV and 20 nA with a 1 μm beam (Supplementary Data Table 4). Magnetite and ilmenite standards from the Smithsonian Museum of Natural History were used to calibrate data. A correction was applied to account for the overlap of the Ti Kβ and V Kα peaks. Average major and trace element uncertainties (1 std. dev.) during electron microprobe sessions were as follows, reported as the percentage of absolute values. Silicate melt and mineral inclusions: ±0.5–1% SiO_2 and Al_2O_3, 2–5% K_2O, Na_2O, CaO, FeO, MgO and TiO_2, 10–15% MnO and P_2O_5, >50% BaO, 15–20% S, and 10–12% F and Cl. Monazite and xenotime mineral inclusions: ±1–4% La_2O_3, Ce_2O_3, Pr_2O_3 and Nd_2O_3, 6–7% Sm_2O_3, 15% Eu_2O_3, 2% Gd_2O_3, 5–10% Tb_2O_3, Dy_2O_3 and Ho_2O_3, 10–15% Tm_2O_3 and Yb_2O_3, 20% Lu_2O_3, 14% Y_2O_3, 3% ThO_2, 0.5% P_2O_5, 7% CaO, 5% SiO_2, >50% Al_2O_3, 5–10% Sc_2O_3. Magnetite and ilmenite mineral inclusions: ±0.5% FeO and TiO_2, 2–4% Al_2O_3 and MnO, 12% V_2O_3, 10–30% ZnO, MgO and Cr_2O_3, >50% CaO, K_2O, Na_2O and NiO.

3.2.3. Ion microprobe analyses

A sensitive high-resolution ion microprobe with reverse geometry (SHRIMP-RG) co-operated by the USGS and Stanford University was used to measure H_2O, REE, Rb, Sr, Y, Nb, Th, and U in silicate melt inclusions (Supplementary Data Table 1). The instrument was operated at 10 kV with an O^{2-} primary ion beam at 0.3–0.8 nA. The spot diameter was ~14–16 μm and the pit depth was ~2 μm. A mass resolving power (M/ΔM) of ~10,000 at 10% peak height was used. The mass table included $^{16}O^1H^+$, $^{30}Si^+$, $^{85}Rb^+$, $^{88}Sr^+$, $^{89}Y^+$, $^{90}Zr^+$, $^{93}Nb^+$, $^{139}La^+$, $^{140}Ce^+$, $^{146}Nd^+$, $^{147}Sm^+$, $^{151}Eu^+$, $^{158}Gd^{16}O^+$, $^{159}Tb^{16}O^+$, $^{162}Dy^{16}O^+$, $^{165}Ho^{16}O^+$, $^{166}Er^{16}O^+$, $^{169}Tm^{16}O^+$, $^{172}Yb^{16}O^+$,

$^{232}Th^{16}O^+$, and $^{238}U^{16}O^+$. Zirconium was included in the run table to monitor and avoid overlap with zircon hosts. Heavy REE, Th and U were measured as oxides to eliminate isobaric interferences. All masses were ratioed to ^{30}Si to account for any drift in the primary beam intensity. Calibration curves were calculated using a linear regression of ^{30}Si-ratioed masses and published concentrations of natural and synthetic glass standards, including Panum (2170, 51, 59), RLS (140, 158, 37, 76–75), and NIST 611 (Macdonald et al., 1992; Hervig et al., 2006; Wright et al., 2012). Melt inclusion SiO_2 concentrations were used to normalize ^{30}Si-ratioed masses. Each calibration curve was constructed using the average and standard deviation of glass standard analyses run throughout the session (typically 5–10 analyses per standard and 20–50 total analyses per calibration curve). The R^2 coefficients for the linear regressions were >0.99 and the uncertainty of the calculated concentrations for the unknown glasses based on the 95% confidence bands of the regressions ranged from 5 to 30% of the absolute values, $\pm$5–10% H_2O, 5–15% REE, 20–30% Rb and Sr, 10–15% Y and Nb, 5–10% Th and U.

In separate analytical sessions, the SHRIMP-RG was used to determine $^{207}Pb/^{206}Pb$ ages and trace elements for zircon hosts (Supplementary Data Table 5). The instrument was operated at 10 kV with an O^{2-} primary ion beam at 3.5–4.5 nA. The spot diameter was $\sim$20–25 μm and the pit depth was $\sim$1.5 μm. A mass resolving power M/ΔM of $\sim$8000–8500 at 10% peak height was used. The mass table included $^{48}Ti^+$, $^{49}Ti^+$, $^{56}Fe^+$, $^{89}Y^+$, $^{139}La^+$, $^{140}Ce^+$, $^{146}Nd^+$, $^{147}Sm^+$, $^{153}Eu^+$, $^{155}Gd^+$, $^{163}Dy^{16}O^+$, $^{166}Er^{16}O^+$, $^{172}Yb^{16}O^+$, a high mass normalizing species ($^{90}Zr_2^{16}O^+$), followed by $^{180}Hf^{16}O^+$, $^{204}Pb^+$, a background measured at 0.045 mass units above the $^{204}Pb^+$ peak, $^{206}Pb^+$, $^{207}Pb^+$, $^{208}Pb^+$, $^{232}Th^+$, $^{238}U^+$, $^{232}Th^{16}O^+$, $^{238}U^{16}O^+$, and $^{238}U^{16}O_2^+$. ^{207}Pb was used to correct measured $^{206}Pb/^{238}U$ for common Pb, whereas ^{204}Pb was used to correct $^{207}Pb/^{206}Pb$. The common Pb correction was based on a model Pb composition from Stacey and Kramers (1975). $^{206}Pb/^{238}U$ ratios were normalized to zircon standards R33 (419.3 Ma) and TEMORA-2 (416.8 Ma) (Black et al., 2004). Trace elements were standardized against MAD-green zircon (Barth and Wooden, 2010), which had average uncertainties (1 std. dev.) of $\pm$3–8% for U and Th, 1–4% for Hf, 5–10% for Y and the heavy REE, 5–15% for the light and middle REE, and 5–10% for Ti and Fe. SHRIMP-RG data were reduced following the methods of Williams (1997) and Ireland and Williams (2003) using Excel and the add-in programs Isoplot 3.76 and Squid 2.51 (Ludwig, 2009, 2012).

A CAMECA ims 1290 ion microprobe at the University of California, Los Angeles (UCLA) was used to determine oxygen isotope compositions for a subset of the zircons for which $^{207}Pb/^{206}Pb$ ages were determined on the SHRIMP-RG (Supplementary Data Table 5). Previous analytical pits were polished away prior to analysis to remove any implanted oxygen and ensure a flat analytical surface (e.g., Kita et al., 2009). The 1290 ion microprobe was operated at 10 kV with a $^{133}Cs+$ primary ion beam at 2 nA, with a spot diameter of $\sim$10 μm. Three Faraday cup detectors were used to simultaneously measure secondary ions of

$^{16}O^-$, $^{16}OH^-$ and $^{18}O^-$. Ratios of $^{18}O/^{16}O$ in unknowns were standardized against R33 ($\delta^{18}O = 5.55‰$, reported relative to Vienna standard mean ocean water (VSMOW)) and TEMORA-2 ($\delta^{18}O = 8.20‰$, VSMOW) (Valley, 2003). R33 and/or TEMORA-2 standards bracketed each set of unknowns, with $\sim$5–10 analyses before and after each set of $\sim$10–15 unknowns; the average of the bracketing standard analyses was used to correct the unknown values. Instrument mass fractionation based on R33 and TEMORA-2 analyses ranged from +0.9 to +2.5‰, averaging +1.5‰, and the external reproducibility (1 std. dev.) ranged from 0.1 to 0.5‰, averaging 0.2‰.

4. RESULTS

4.1. Zircon-hosted silicate melt inclusion geochemistry

4.1.1. Major elements

Compositions of melt inclusions span from trachydacite to high-silica rhyolite ($\sim$63–79 wt% SiO_2), with the least-evolved melt inclusions found in Pea Ridge samples (Fig. 2a, Supplementary Data Table 1). In addition to Pea Ridge, a couple of melt inclusions in Bourbon sample Bourb-204 are trachydacitic (Fig. 2a). Melt inclusions span from less- to more-evolved compositions relative to whole-rocks, though whole-rock samples for Bourbon (Bourb-204) and Eminence (MO14-007) are at the lower and higher end of the melt inclusion SiO_2 ranges, respectively (Fig. 2a). About half of the Pea Ridge melt inclusions are alkalic ($\sim$8.3–11.7 wt% $Na_2O + K_2O$ and $\sim$8.4–10.8 wt% $Na_2O + K_2O$-CaO; Fig. 2b) and they demonstrate a statistically significant trend of decreasing total alkalis with silica (Fig. 2a inset). The majority of melt inclusions from other samples fall within the alkali-calcic and calc-alkalic fields (Fig. 2b). Bourbon melt inclusions have distinctly higher CaO and lower K_2O than other samples for the same SiO_2 ranges, spanning the alkali-calcic to calcic fields (Fig. 2b, Supplementary Data Table 1).

Most analyzed melt inclusions are ferran, with FeO/FeO + MgO of $\sim$0.8–1.0, and slightly metaluminous to moderately peraluminous, with molar $Al_2O_3/(Na_2O + K_2O + CaO)$ of $\sim$ 0.9–1.1 (Supplementary Data Table 1). Pea Ridge melt inclusions generally have higher FeO ($\sim$1.5–4 wt%) and TiO_2 ($\sim$0.1–0.3 wt%) compared to other samples (Supplementary Data Table 1). The least-evolved (<70 wt% SiO_2) Pea Ridge melt inclusions, and all but one Bourbon melt inclusion, have distinctly higher Al_2O_3 ($\sim$13–17 wt%) than the most-evolved Pea Ride melt inclusions and the majority of Eminence melt inclusions ($\sim$11–13 wt%) (Supplementary Data Table 1). Pea Ridge and Bourbon melt inclusions have overlapping ranges in alumina saturation indices plots, straddling the metaluminous to peraluminous fields, and while Pea Ridge melt inclusions partly overlap with Eminence, Bourbon forms a separate array. Pea Ridge melt inclusions have Al_2O_3 contents that decrease systematically with SiO_2 (Supplementary Data Table 1). Eminence sample MO14-009 also demonstrates a decrease in Al_2O_3 with SiO_2, though over a more restricted range of SiO_2, whereas other samples do not exhibit this trend (Supplementary Data Table 1). There were no
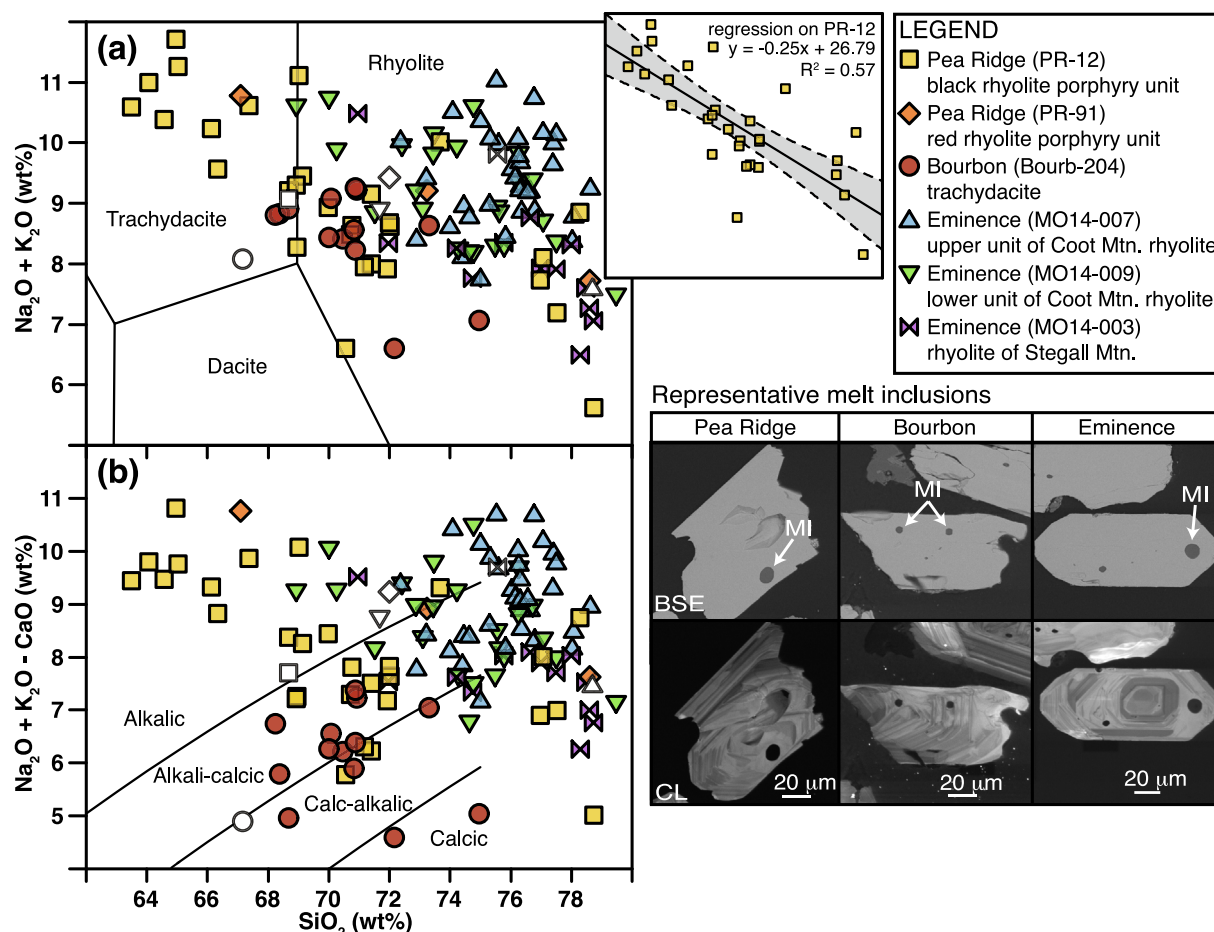
Fig. 2. Major element geochemistry of zircon-hosted melt inclusions determined by electron microprobe, including (a) total alkali-silica diagram and (b) modified alkali-lime-silica diagram. White filled symbols of the same type identified in the legend for each sample show the whole-rock compositions of the same or equivalent samples. Upper inset shows a linear regression (solid black line) and 95% confidence band (gray field bounded by dashed black lines) for melt inclusions from sample PR-12, showing a statistically significant correlation between total alkalis and silica content ($R^2 = 0.57$). Lower inset shows scanning electron microprobe images of representative melt inclusions (MI) in backscattered electrons (BSE) and cathodoluminescence (CL).

differences observed for major element concentrations between homogenized and non-homogenized melt inclusions for the investigated samples (Supplementary Data Table 1).

4.1.2. Volatiles and trace elements

Five melt inclusions each from Pea Ridge sample PR-12 and Eminence sample MO14-007 were large enough to determine H_2O contents using the SHRIMP-RG ion microprobe. Pea Ridge melt inclusions span from 2.06 to 3.19 wt% H_2O (average of 2.52 wt%) and Eminence melt inclusions span from 3.43 to 4.72 wt% H_2O (average of 3.91 wt%) (Supplementary Data Table 1). H_2O did not vary systematically with SiO_2 content in either sample (Supplementary Data Table 1). Chlorine, P, S, ±F contents were determined by electron microprobe for all melt inclusions for which major element data were collected. Chlorine spans from low to very high, ~100–9000 ppm, with the highest Cl contents found in Pea Ridge and Bourbon melt inclusions (Fig. 3, Supplementary Data Table 1). Pea Ridge melt

inclusions define a trend of decreasing Cl with increasing SiO_2 (Fig. 3). Bourbon melt inclusions, which occupy a narrower range of SiO_2, define an overlapping but steeper trend (Fig. 3). Of the Eminence melt inclusions, which typically have <1000 ppm Cl, there are a few from sample MO14-003 with higher Cl of ~2000 ppm (Fig. 3). P (~0–300 ppm), S (~0–200 ppm) and F (~0–4000 ppm) are generally low to moderate for all melt inclusions from Pea Ridge, Bourbon and Eminence (Supplementary Data Table 1).

Trace elements including REE, Rb, Sr, Y, Nb, Th, and U were also measured by SHRIMP-RG ion microprobe for sufficiently large Pea Ridge and Eminence melt inclusions (Supplementary Data Table 1). Pea Ridge melt inclusions have chondrite-normalized REE concentrations that are very similar to those determined for whole-rocks for Pea Ridge host rhyolites (Fig. 4, Ayuso et al., 2016; Day et al., 2016). Pea Ridge breccia pipes have a large range in REE concentrations, from barren (<1000× chondrite) to extremely enriched (>100,000× chondrite) (Ayuso
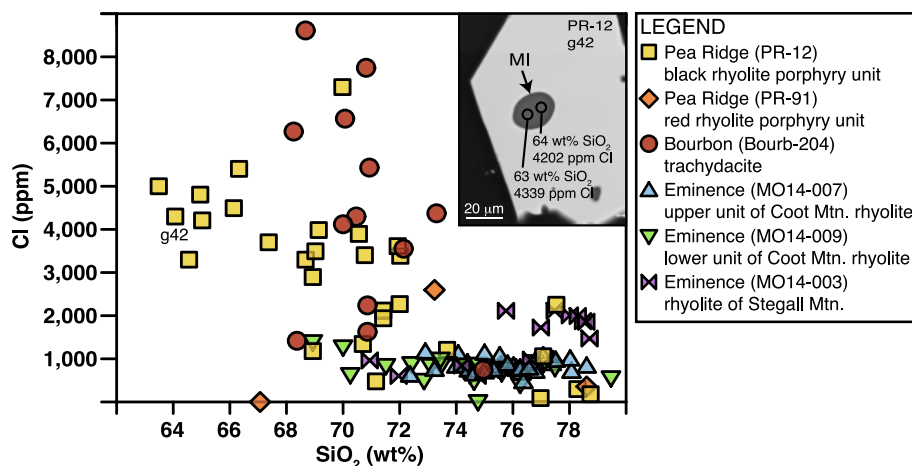
Fig. 3. Chlorine versus silica concentrations in zircon-hosted melt inclusions determined by electron microprobe. Inset shows a scanning electron microprobe image in backscattered electrons of a melt inclusion (MI) in Pea Ridge sample PR-12, with data annotated for adjacent analytical spots; the grain is labeled in the main panel.
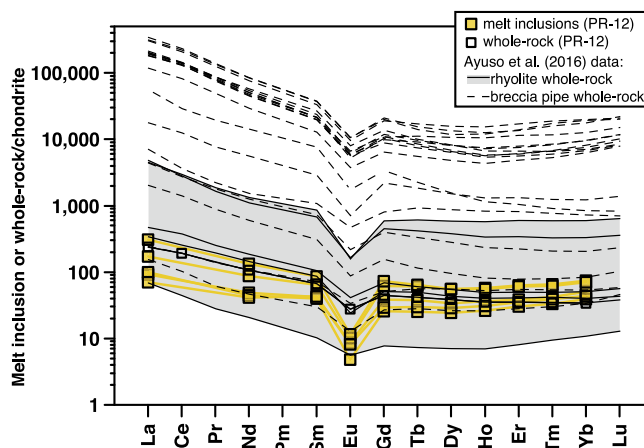

Fig. 4. REE concentrations in zircon-hosted Pea Ridge melt inclusions determined by ion microprobe. Whole-rock data for Pea Ridge rhyolites and breccia pipes are from Ayuso et al. (2016) and the gray shading demarcates the whole-rock rhyolite field. REE for melt inclusions and whole-rocks are normalized to the chondrite values of McDonough and Sun (1995).

et al., 2016); Pea Ridge melt inclusions fall at the lower end of this range (Fig. 4). Though REE concentrations generally decrease with increasing SiO_2 in Pea Ridge inclusions, this trend is less well-defined for Eu (Supplementary Data Table 1). Eminence melt inclusions have similar REE concentrations to Pea Ridge inclusions, but with lower Eu ($\sim$0.2–0.4 ppm for Eminence vs. $\sim$0.3–0.7 ppm for Pea Ridge). Rb/Sr ratios are also discernably higher for Eminence ($\sim$8–13) compared to Pea Ridge ($\sim$4–10) inclusions (Supplementary Data Table 1). A tectonic discrimination diagram using Rb, Y, and Nb indicates that Pea Ridge melt inclusions span the within-plate to volcanic arc granite fields, whereas Eminence melt inclusions straddle the volcanic arc and syn-collisional granite fields (Fig. 5). Similar to the observation for major elements, volatile and trace element concentrations did not systematically vary between homogenized and non-homogenized melt inclusions (Supplementary Data Table 1).

4.1.3. Intensive parameters

Pressures were estimated using normative components of quartz, albite, and orthoclase for melt inclusion compositions, restricted to those with 70–78 wt% SiO_2 for the haplogranite ternary projection (Fig. 6a). Pea Ridge and Bourbon melt inclusions span the largest ranges, from $\sim$0.5 to 10 kbar, and have trends of greater normative quartz and orthoclase relative to albite at lower pressures. Eminence samples cluster more tightly at the lower end of this pressure range and do not define normative trends. Pressure to depth conversions using an average density of 2.64 gm/cm^3 for basement rocks in the St. Francois Mountains terrane (McCafferty et al., 2016) corresponds to $\sim$3.86 km/kbar. For average pressures of $\sim$3–5 kbar for Bourbon, $\sim$2–3 kbar for Pea Ridge and Eminence (Coot Mountain rhyolites), and $\sim$1–2 kbar for the Eminence rhyolite of Stegall Mountain, the corresponding depths are $\sim$11–19 km, $\sim$7–12 km, and $\sim$3–8 km, respectively. We
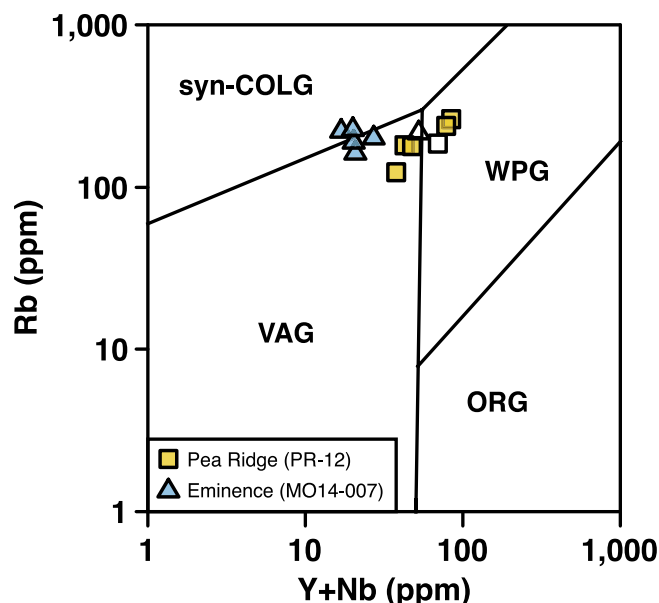
Fig. 5. Rb versus Y + Nb discrimination diagram for tectonic settings of granitic magmas (after Pearce et al., 1984), with zircon-hosted melt inclusion data for Pea Ridge and Eminence samples determined by ion microprobe. Open symbols of the same type show the sample whole-rock compositions. WPG = within-plate granite, VAG = volcanic arc granite, syn-COLG = syncollision, ORG = orogenic granite.

note that including normative anorthite would shift the cotectic curves to higher pressures (cf. Wilke et al., 2017). Though this effect is expected to be minimal for most melt inclusions with <4 wt% normative anorthite, Bourbon melt inclusions commonly have >5 wt% normative anorthite and may therefore have underestimated pressures.

Temperatures were calculated for melt inclusion compositions using the Rhyolite-MELTS thermodynamic modeling software of Gualda et al. (2012) (Fig. 6b). Rhyolite-MELTS was calibrated for trachydacite to high-silica rhyolite compositions and is therefore suitable for all melt inclusions in this study. Average pressures used in the modeling were 4 kbar (Bourbon), 2.5 kbar (Pea Ridge and Eminence Coot Mountain rhyolites), and 1.5 kbar (Eminence rhyolite of Stegall Mountain), as constrained from the haplogranite ternary pressure estimates (Fig. 6a). Average H_2O contents used in the modeling were 2.5 wt% (Bourbon, Pea Ridge) and 3.9 wt% (Eminence), constrained by our new SHRIMP-RG volatile data. Bourbon melt inclusions have the highest calculated liquidus temperatures, spanning from ~935 to 1020 °C, with a mean of ~975 °C. Pea Ridge melt inclusions span the largest range, from ~850 to 975 °C, with a mean of ~920 °C. Eminence melt inclusions have more restricted ranges of ~780–875 °C, with a mean of ~825 °C. For all samples, the means are very close to the median values and do not indicate significant skewing of temperature data (Fig. 6b).

4.2. Zircon-hosted mineral inclusion geochemistry

4.2.1. Silicate mineral inclusions

In addition to silicate melt inclusions, silicate mineral inclusions are also ubiquitous in Pea Ridge, Bourbon, and Eminence zircons, with quartz, alkali feldspar, and

phengitic mica being the most common (Fig. 7, Supplementary Data Table 2). A small proportion of the silicate mineral inclusions have euhedral shapes, but most are subrounded to rounded, and some appear to be in-filled dissolution features. Patchy mixtures of silicate minerals are observed in some cases. Quartz inclusions have Ti contents that range from ~0 to 500 ppm, spanning from likely hydrothermal (~0–50 ppm Ti) to igneous (~100–500 ppm Ti) (cf. Hofstra et al., 2016). Rutile intergrowths with quartz have been documented in hydrothermal quartz for sample PR-12 ('black porphyry' unit of Hofstra et al., 2016), but were not observed in the zircon-hosted quartz inclusions of this study. Alkali feldspar inclusions have Na_2O contents that range from ~0 to 2.3 wt%; the lower end of this range (<1 wt% Na_2O) overlaps compositions of hydrothermal alkali feldspar determined for Pea Ridge porphyry units, whereas a few with ~1.4–2.3 wt% Na_2O are intermediate between hydrothermal and igneous alkali feldspar compositions. Mica inclusions have a phengite composition, with ~4.3–6.7 wt% FeO and ~1.3–3.6 wt% MgO.

4.2.2. Phosphate mineral inclusions

Apatite, monazite, and xenotime are phosphate mineral inclusion types observed in Pea Ridge, Bourbon, and Eminence zircons. Monazite and xenotime inclusions are particularly abundant in zircons from Pea Ridge sample PR-91 (Fig. 8, Supplementary Data Table 3). These inclusions tend to occur in irregular re-entrants or dissolution features that cross-cut primary zircon growth zones and are associated with alkali feldspar and phengite (Fig. 8 insets). Monazite and xenotime are commonly intergrown or attached (Fig. 8b inset), and monazite was also observed to occur as rims on some anhedral zircon grains. REE
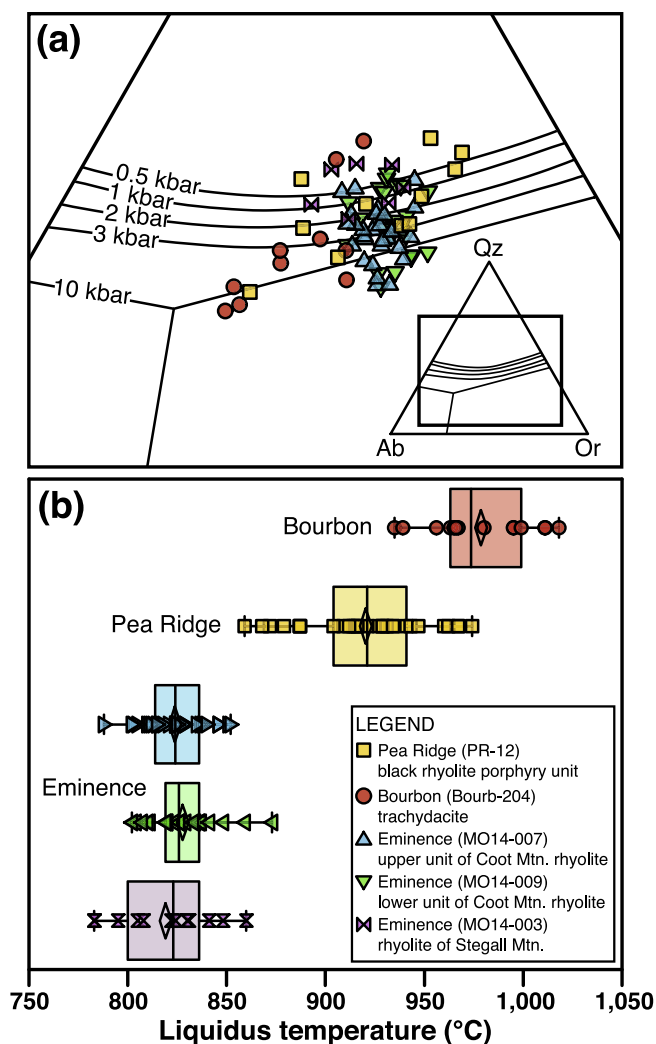
Fig. 6. Intensive parameters for zircon-hosted melt inclusions. (a) Pressures based on normative quartz (Qz), albite (Ab), and orthoclase (Or), with cotectic curves from 0.5 to 10 kbar labeled in the haplogranite ternary. The lower right inset shows the area of the Qz-Ab-Or ternary that is represented in the plot. (b) Liquidus temperatures calculated using Rhyolite-MELTS thermodynamic modeling software (Gualda et al., 2012). Box and whisker plots show the upper and lower quartiles (outer box boundaries), the medians (vertical black lines), and the means (open diamond symbols) for each sample group.

concentrations of the monazite and xenotime inclusions overlap the higher end of the ranges determined for monazite and xenotime in Pea Ridge ore zones (Fig. 8).

4.2.3. Iron oxide mineral inclusions

Magnetite and ilmenite mineral inclusions are ubiquitous in Pea Ridge, Bourbon, and Eminence zircons, but only one Pea Ridge sample (PR-12) has fresh inclusions of both magnetite and ilmenite (Fig. 9; Supplementary Data Table 4). Magnetite inclusions in other samples have pervasive ilmenite oxy-exsolution textures. In PR-12 zircons, magnetite inclusions have ~72.7–73.8 wt% FeO and ~14.5–15.6 wt% TiO_2 and ilmenite inclusions have ~43.5–46.7 wt% FeO and ~48.2–49.2 wt% TiO_2 (Fig. 9, Supplementary Data Table 4). Magnetite inclusions have ~1.2–1.4 wt% Al_2O_3, ~0.3–0.5 wt% MnO, and ~0.2–0.3 wt% V_2O_3 and ilmenite inclusions have ~2–6 wt% MnO

(Supplementary Data Table 4). Ilmenite and magnetite compositions correspond to an equilibrium temperature of ~780–860 °C, oxygen fugacity of −0.8 to −1.84 (log fO_2 ΔNNO), and Ti activity ($aTiO_2$) of 0.5, using the two-oxide geothermometer and oxygen-barometer of Ghiorso and Evans (2008).

4.3. Zircon geochronology

Pea Ridge, Bourbon, and Eminence zircons demonstrate a broad spread in Mesoproterozoic $^{207}Pb/^{206}Pb$ ages, as illustrated by concordia and weighted average age plots and calculations for each sample (Fig. 10, Supplementary Data Table 5). Pea Ridge sample PR-12 has a concordia age of 1456 ± 9 Ma and an identical weighted average age of 1456 ± 12 Ma (Fig. 10a). One significantly older (>1550 Ma) zircon core was found in PR-12, with dates
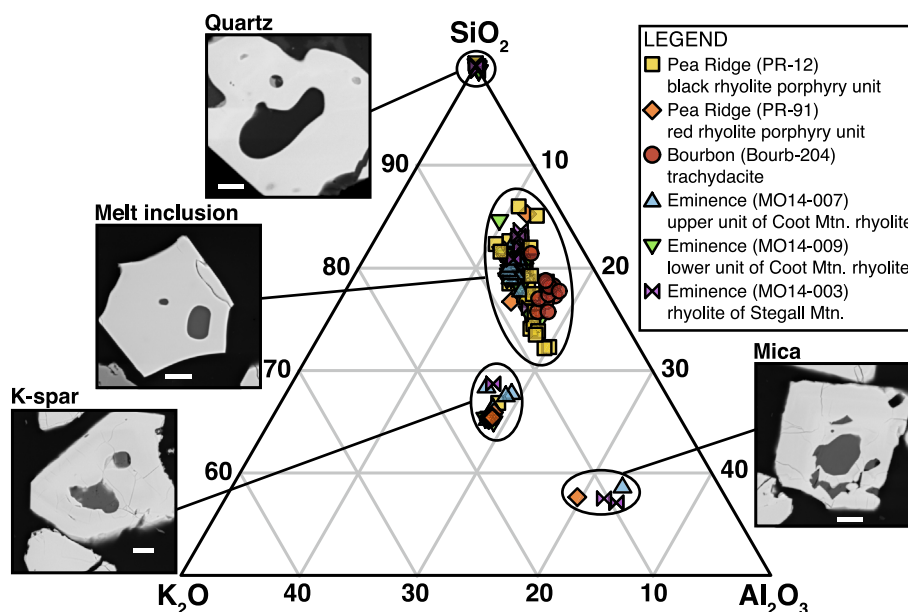
Fig. 7. Zircon-hosted silicate minerals and melt inclusions shown on a SiO_2-K_2O-Al_2O_3 ternary plot, where oxides are in wt%. Gray lines show 10 wt% increments; plot is truncated at 50–100 wt% SiO_2, and 0–50 wt% K_2O and Al_2O_3. Insets are scanning electron microprobe images of representative inclusion types in backscattered electrons; the white bar at the bottom of each image is 20 μm.

of 1585 ± 43 Ma and 1597 ± 32 Ma that were determined for adjacent spots during two analytical sessions (Fig. 10a, inset). Zircons from Pea Ridge sample PR-91 have a concordia age of 1467 ± 13 Ma and a weighted average age of 1462 ± 11 Ma, which is older, though overlapping within error, of the ages determined for PR-12 (Fig. 10a and b). Unlike PR-12, most zircon grains in PR-91 are discordant, and many exhibit dissolution textures and irregular CL that suggests hydrothermal overprinting. Zircons from Bourbon sample Bourb-204 have the widest spread in ages and overall oldest dates, with a concordia age of 1499 ± 11 Ma and a weighted average age of 1486 ± 16 Ma (Fig. 10c). Four >1550 Ma inherited cores were found in Bourb-204, with the oldest core at 1618 ± 73, mantled by a younger rim at 1442 ± 41 Ma (Fig. 10c inset). Eminence zircons from the upper unit of Coot Mountain rhyolite, sample MO14-007, have a concordia age of 1452 ± 14 Ma and a weighted average age of 1469 ± 17 Ma (Fig. 10d), and from the lower unit of Coot Mountain rhyolite, sample MO14-009, have a concordia age of 1460 ± 10 Ma and a weighted average age of 1458 ± 15 Ma (Fig. 10e).

4.4. Zircon trace element geochemistry

Actinide (U, Th) concentrations are low to moderate for most Pea Ridge and Bourbon zircons, with U < 300 ppm and Th < 200 ppm (Supplementary Data Table 5). Notable exceptions are zircons from Pea Ridge sample PR-91 and discordant zircons from samples PR-91 and PR-12, which have U contents up to ~800 ppm and Th up to ~550 ppm. Many of these discordant zircons also have very high Fe (>30 ppm) (Supplementary Data Table 5). Eminence zircons have overlapping but generally lower U (<200 ppm) and Th (<100 ppm). Th/U ratios span from

~0.25 to 0.45 for Eminence zircons and ~0.35–0.75 for Pea Ridge and Bourbon zircons (Fig. 11a). Concentrations of lanthanide REE (La, Ce, Nd, Sm, Eu, Gd, Dy, Er, Yb) are higher in Pea Ridge and Bourbon zircons compared to Eminence zircons, with the highest concentrations observed in discordant and texturally complex zircons of sample PR-91 (Fig. 11b). Europium concentrations in Eminence zircons are low (<0.5 ppm), whereas those from Pea Ridge and Bourbon zircons extend up to ~1.5 ppm (Fig. 11a). Negative Eu anomalies are apparent in REE spectra for all zircon samples (Fig. 11 insets). The highest REE concentrations for the heavy REE in Pea Ridge and Bourbon zircons are up to ~1000–10,000× chondrite values (Fig. 11 insets).

Titanium concentrations are highest for Bourbon zircons (~50–100 ppm), followed by zircons from Pea Ridge sample PR-12 (~12–80 ppm), Eminence zircons (~10–50 ppm), and are lowest for zircons from Pea Ridge sample PR-91 (~3–12 ppm) (Fig. 12). Ti-in-zircon temperatures determined using the geothermometer of Ferry and Watson (2007) correspond to average temperatures of ~970 °C for Bourbon, ~880 °C for Pea Ridge (PR-12), ~800–825 °C for Eminence, and ~690 °C for Pea Ridge sample PR-91. A TiO_2 activity ($aTiO_2$) of 1 was used for these calculations; temperatures shift upwards by ~70–100 °C if using $aTiO_2$ of 0.5 (Fig. 12). The Ti-in-zircon temperatures are within 0–40 °C of mean and median liquidus temperatures determined for melt inclusion compositions using Rhyolite-MELTS (Fig. 6b).

4.5. Zircon oxygen isotope geochemistry

Oxygen isotope data were collected for a subset of zircons analyzed for ^{207}Pb/^{206}Pb ages and trace element concentrations (Fig. 13, Supplementary Data Table 5). While
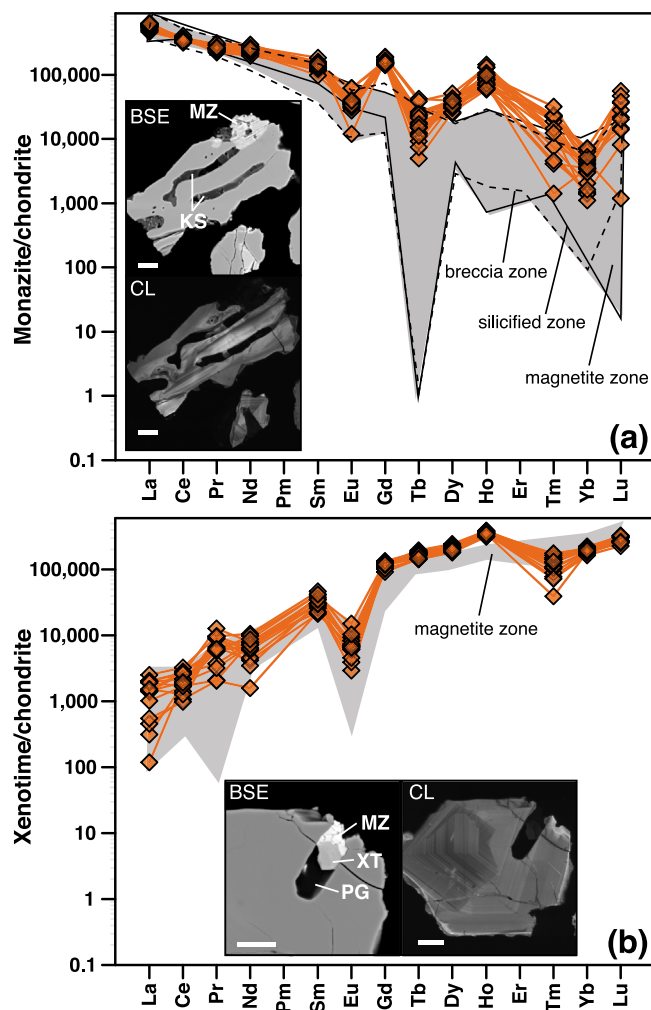
Fig. 8. REE concentrations of (a) monazite and (b) xenotime inclusions in Pea Ridge (PR-91) zircons determined by electron microprobe. Monazite and xenotime REE data for different Pea Ridge ore zones are from Harlov et al. (2016) and shown by the shaded and outlined fields. REE concentrations are normalized to the chondrite values of McDonough and Sun (1995). Insets show scanning electron microprobe images of representative inclusions in backscattered electrons (BSE) and cathodoluminescence (CL); the white bar at the bottom of each image is 20 μm; MZ = monazite, XT = xenotime, KS = alkali feldspar, PG = phengite.

zircon $^{207}Pb/^{206}Pb$ age data overlap for all samples, $\delta^{18}O$ values define separate fields for Pea Ridge and Bourbon ($\delta^{18}O_{zircon}$ = 5.5–7.9‰) relative to Eminence ($\delta^{18}O_{zircon}$ = 8.3–9.6‰) (Fig. 13). Whereas Pea Ridge and Bourbon zircons span from mantle to crustal values, Eminence zircons have very high- $\delta^{18}O$ values that require a significant supracrustal (sedimentary) component (e.g., Valley et al., 2005). The oxygen isotope range of Pea Ridge and Bourbon zircons is identical to the range determined by King et al. (2008) for bulk zircons from the Butler Hill and Taum Sauk calderas in the central St. Francois Mountains terrane (Fig. 1). A couple of the inherited (>1550 Ma) zircon cores from Pea Ridge and Bourbon samples have lower $\delta^{18}O$ values ($\delta^{18}O_{zircon}$ = 5.5–6.0‰) that support a mantle origin, whereas other >1550 Ma grains have much higher values ($\delta^{18}O_{zircon}$ = 6.7–7.2‰) that are distinctly crustal, with equilibrium magma (melt) $\delta^{18}O$ values of ~8.0–8.5‰, based on $\Delta^{18}O_{melt-zircon} \approx 1.3$‰ at 900 °C (Trail et al., 2009).

Discordant zircons have $\delta^{18}O$ values within the same ranges as those for concordant zircons, supporting oxygen isotopic stability in zircon despite evidence for hydrothermal overprinting (e.g., Bindeman et al. 2018).

5. DISCUSSION

5.1. Igneous petrogenesis

Our new melt inclusion data indicate that primary magmas at Pea Ridge were naturally alkalic and evolved towards less alkalic compositions (Fig. 2). The prevailing assumption that most whole-rock compositions were affected by sodic and potassic alteration of the Pea Ridge IOA system needs to be reconsidered in light of these new data. Previous workers used trace element ratios, such as Zr/Ti and Nb/Y, as proxies for melt alkalinity and concluded that Pea Ridge magmas were subalkaline as opposed
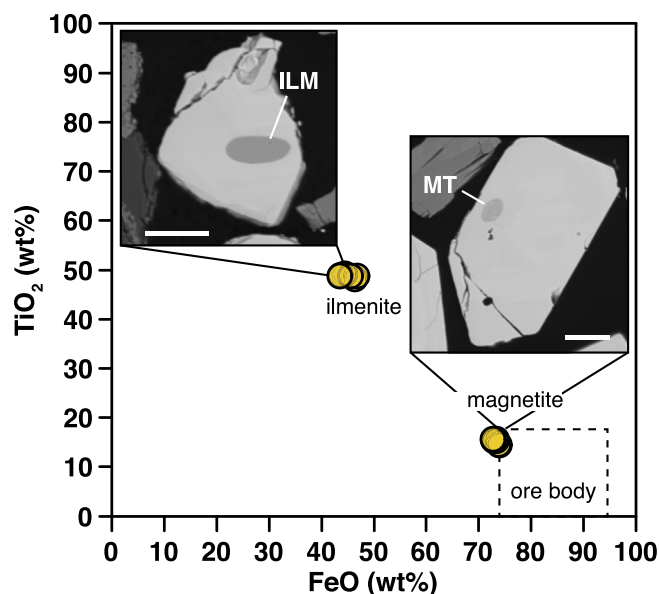
Fig. 9. Iron and Ti concentrations in magnetite and ilmenite inclusions in Pea Ridge (PR-12) zircons determined by electron microprobe. The dashed box shows the range of magnetite compositions in the Pea Ridge magnetite ore body (Childress et al., 2016). Insets are scanning electron microprobe images of representative inclusions in backscattered electrons; the white bar at the bottom of each image is 20 μm; MT = magnetite, ILM = ilmenite.

to alkaline (e.g., Day et al., 2016; Ayuso et al., 2016). Whole-rock analyses with high total alkalis that were within the range of the new melt inclusion data were assumed to be altered and were not considered in the evaluation of the Pea Ridge magmatic system. In the least-evolved Pea Ridge melt inclusions, it is K that is high (~7 wt% K_2O), whereas Na is within a range more typical of silicic magmas (~3–4 wt% Na_2O) (Supplementary Data Table 1). Chlorine concentrations in the Pea Ridge melt inclusions are also extraordinarily high, ~5000 ppm in the least-evolved inclusions (Fig. 3), which far exceeds typical concentrations in rhyodacitic magmas (<500 ppm) (GEOROC database). Melt inclusions from the adjacent Bourbon magmatic have comparably high Cl, and like Pea Ridge, exhibit a trend of decreasing Cl with increasing SiO_2 (Fig. 3).

The high K and Cl in the least-evolved melt inclusions are consistent with a metasomatized lithospheric mantle component in Pea Ridge magmas (e.g., Ayuso et al., 2016). However, our data also indicate that assimilation of crust, including cratonic (>1550 Ma) crustal material, was central to magma genesis. Inherited (>1550 Ma) zircon xenocrysts and high- $\delta^{18}O$ crustal signatures of autocrystic zircon in Pea Ridge and Bourbon samples provide unequivocal evidence of crustal assimilation (Figs. 10 and 13). We note that Sm-Nd model ages determined by Ayuso et al. (2016) for Pea Ridge host rocks also trend towards older 1.55–1.65 Ga crustal residence ages, which the authors suggested may be due to mixing of cratonal material with younger juvenile source rocks. Melting and assimilation of heterogeneous mantle and crustal components in a back-arc setting as the locus of subduction migrated in the St. Francois Mountains terrane is a

plausible model (e.g., Mengue et al., 2002). The decrease of K_2O and Al_2O_3 with increasing SiO_2 is consistent with feldspar fractionation in an intermediate to felsic melt. Bourbon melt inclusions have lower K (~4–6 wt% K_2O) and higher Ca (~2–4 wt% CaO), and define a trend of decreasing CaO (and a more subtle trend of decreasing K_2O) with SiO_2 (Supplementary Data Table 1), consistent with a more significant role of plagioclase fractionation in this system.

Haplogranite ternary projections and Rhyolite-MELTS liquidus modeling indicate that Bourbon and Pea Ridge melt inclusions have the highest equilibrium pressures and temperatures (Fig. 6), with a few inclusions that extend up to ~10 kbar and temperatures up to ~1000 °C, supporting a model in which melting began at the lower crust-mantle boundary and migrated upwards to mid-crustal levels where magma chambers were assembled and continued to evolve through assimilation-fractional crystallization (AFC) processes. Water contents of Pea Ridge melt inclusions are low to moderate and oxygen fugacity constraints indicate that the magmas were reduced to mildly oxidized (~2.5 wt% H_2O, log fO_2 −0.8 to −1.84 ΔNNO). Eminence melt inclusions lie at the more-evolved end of the compositional spectrum (Fig. 2), with lower Eu contents and higher Rb/Sr ratios that indicate a larger degree of feldspar fractionation. Average equilibrium pressures and temperatures are likewise lower, at <3 kbar and <850 °C (Fig. 6), and water contents higher (~4 wt% H_2O). Zircons from Eminence samples have distinctively high- $\delta^{18}O$ (supracrustal) values that point to shallow assimilation of sedimentary sources. These magmas lack any evidence of either a metasomatized mantle component or inherited cratonal material.
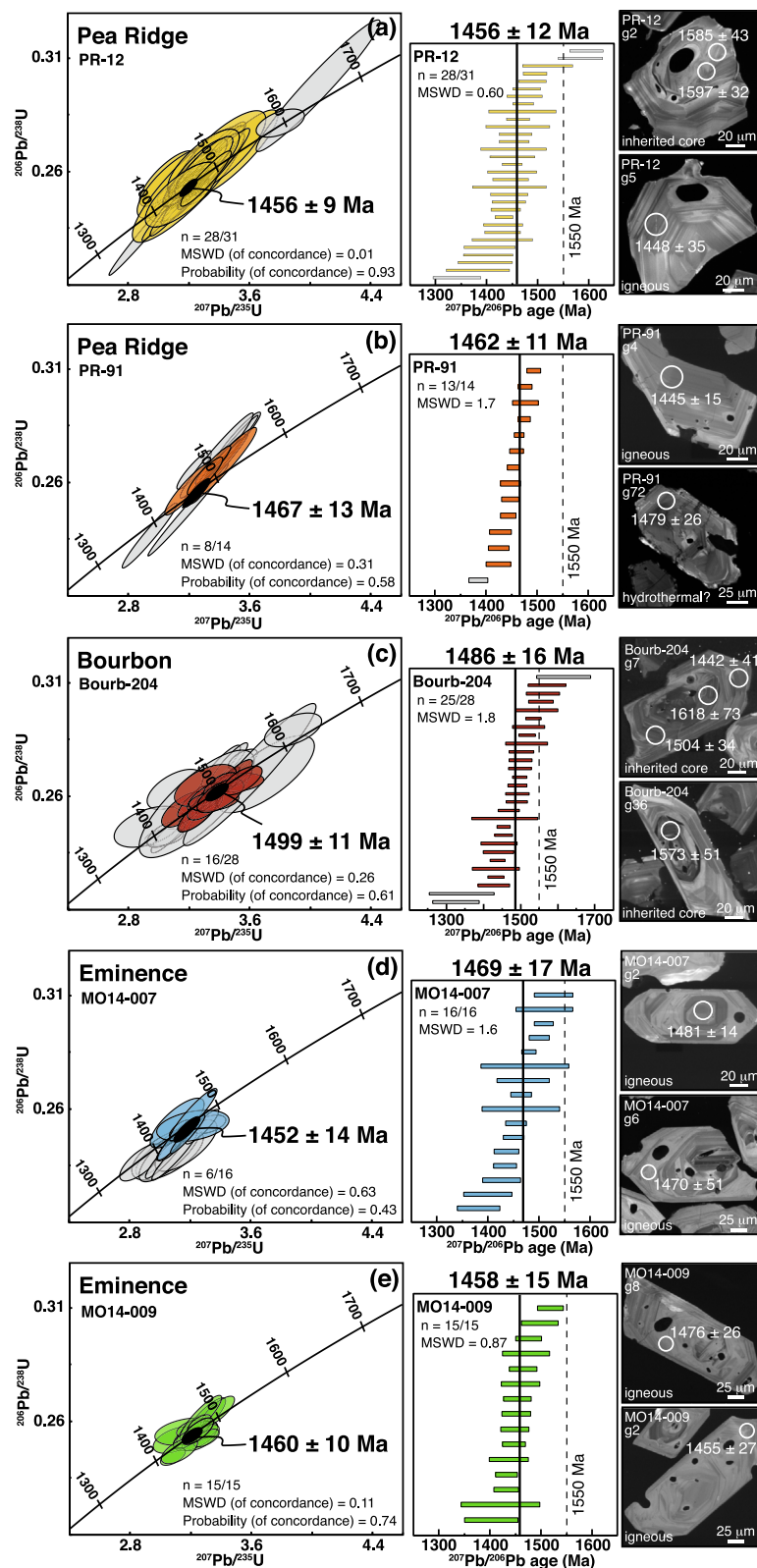
Fig. 10. Geochronology summary of zircon samples dated by SHRIMP-RG ion microprobe. Panels to the left show $^{206}Pb/^{238}U$-$^{207}Pb/^{235}U$ concordia ages and panels to the right show weighted average $^{207}Pb/^{206}Pb$ ages. Ages for each sample are shown by the black ellipses and black vertical lines and labeled in bold text. Gray ellipses and gray bars show the data points that were excluded from age calculations. Only statistically concordant age data are plotted. Error ellipses are 1σ. Concordia ages are reported to 2σ with decay constant errors included and weighted average ages are reported to 95% confidence. Plotting and calculations were performed using Isoplot, v. 3.76 (Ludwig, 2012). Cathodoluminescence scanning electron microprobe images to the right show selected features of zircons for each sample.
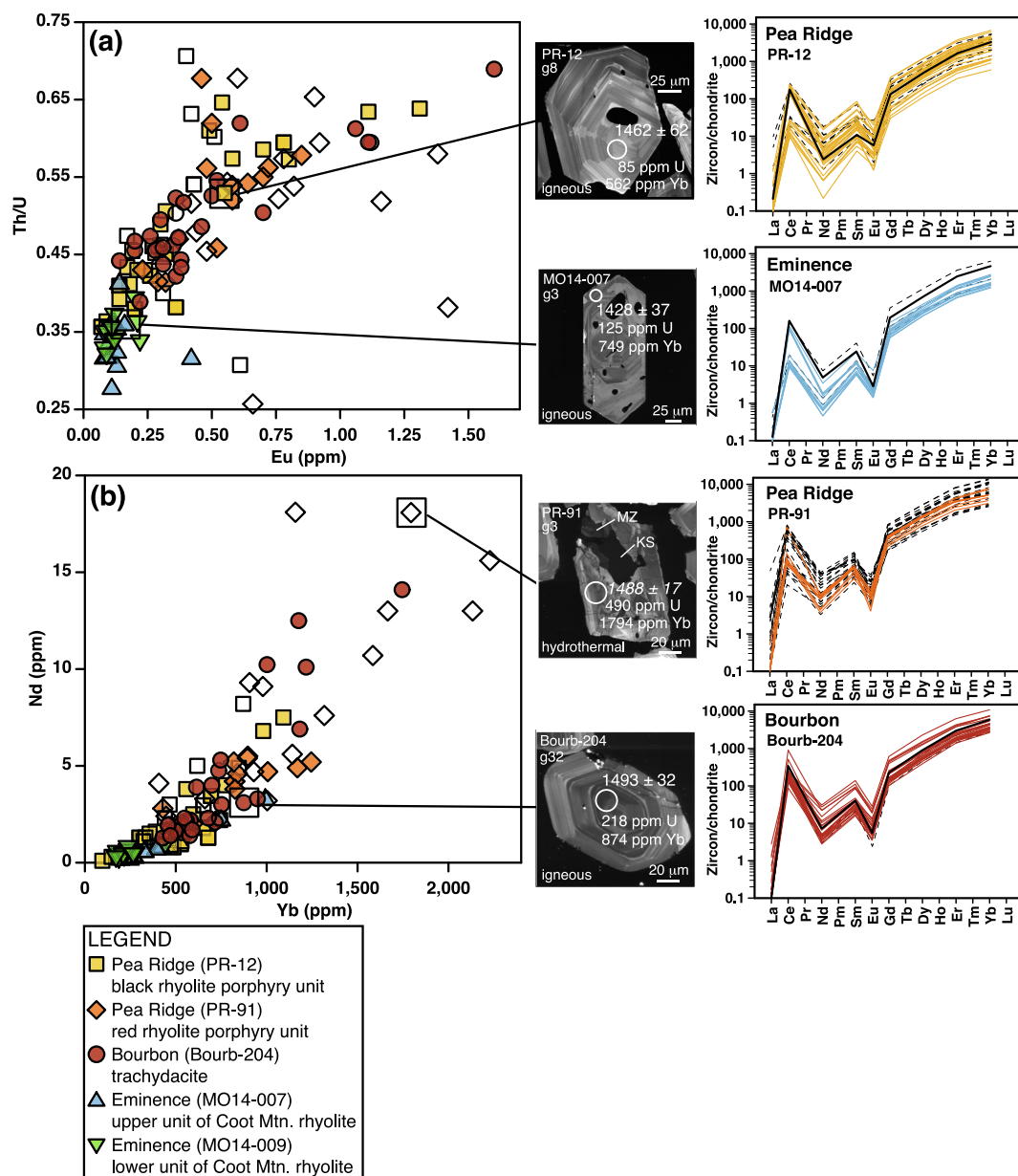
Fig. 11. Zircon U, Th, and REE concentrations determined by SHRIMP-RG ion microprobe. Open symbols of the same type identified in the legend indicate statistically discordant analyses. Cathodoluminescence scanning electron microprobe images to the right show representative zircons with $^{207}Pb/^{206}Pb$ ages, U, and Yb concentrations annotated; for PR-91, italics denotes a discordant age and MZ = monazite and KS = alkali feldspar. The rightmost panels show chondrite-normalized REE plots for each sample; thin dashed black lines indicate discordant analyses and bold black lines show the representative analysis depicted in the plots and images.

5.2. Transition from igneous to hydrothermal regime

In addition to zircons with melt inclusions and textures that are consistent with an igneous origin, Pea Ridge zircons have silicate and phosphate mineral inclusions and textural and geochemical evidence that point to hydrothermal overprinting. Inclusions of low-Ti quartz (Ti $\sim$0–50 ppm), low-Na alkali feldspar ($Na_2O < 1$ wt%), and high-Fe and -Mg phengitic mica (FeO and MgO $\sim$3–4 wt %) are consistent with a hydrothermal origin (Figs. 7 and 8). The phengitic mica phase has a geochemical signature

similar to hydrothermal phengites described in the Olympic Dam IOCG deposit (Tappert et al., 2013). Monazite and xenotime mineral inclusions are commonly associated with alkali feldspar and phengite, and they have a geochemical composition that is within the same range as those documented in different fluorapatite-bearing alteration zones of the Pea Ridge IOA deposit, including comparably high REE concentrations (Fig. 8) and low-Th ($ThO_2 < 2$ wt%) (Harlov et al., 2016). Silicate and phosphate inclusions commonly occur in dissolution features that cross-cut primary zircon growth zones (e.g., insets of Fig. 8). The data
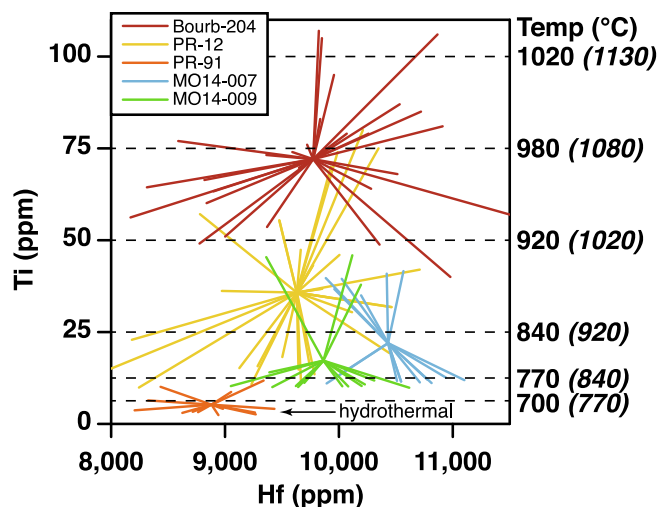
Fig. 12. Zircon Ti and Hf concentrations determined by SHRIMP-RG ion microprobe. Colored lines connect individual data points to the means of each sample group. Ti-in-zircon temperatures were calculated using the calibration of Ferry and Watson (2007), using $aTiO_2 = 1$ (bold) and $aTiO_2 = 0.5$ (bold italics in parentheses). Temperatures are annotated to the nearest 10 °C, with dashed black lines that connect to corresponding Ti concentrations. Only statistically concordant data were used.
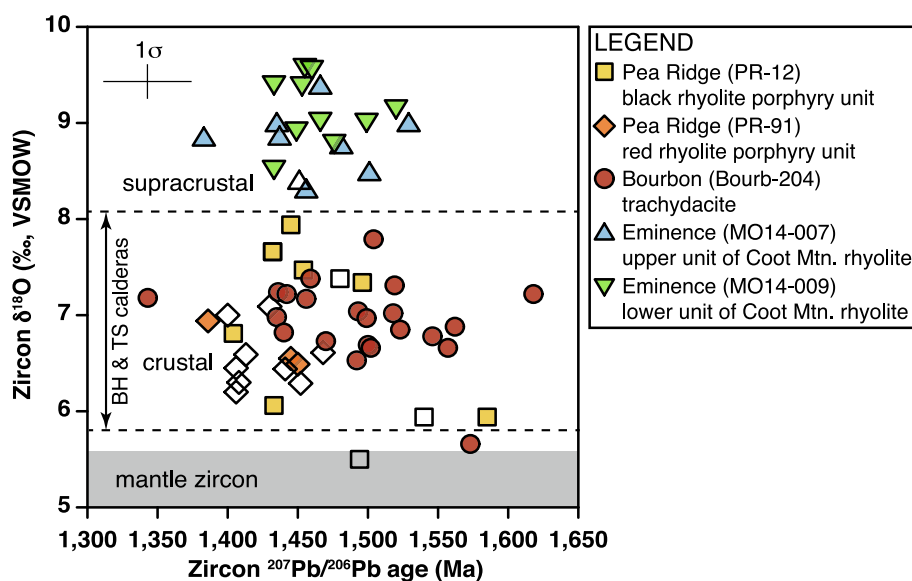

Fig. 13. Zircon $\delta^{18}O$ values and $^{207}Pb/^{206}Pb$ ages determined by ion microprobe. Open symbols of the same type identified in the legend indicate statistically discordant analyses. The average 1σ uncertainty for data points is shown in the upper left. The gray shading shows the field for mantle zircon: $\delta^{18}O = 5.3 \pm 0.3‰$ (Valley et al., 1998). The range of zircon $\delta^{18}O$ values reported by King et al. (2008) for the Butler Hill and Taum Sauk calderas in the St. Francois Mountains terrane is indicated by the vertical arrow and bounded by dashed lines. All $\delta^{18}O$ values were calculated relative to VSMOW = Vienna standard mean ocean water.

support a dissolution-reprecipitation process (e.g., Geisler et al., 2007) in which zircon was dissolved by magmatic-hydrothermal fluids, followed by precipitation of phosphates, akali feldspar, and phengitic mica. Alkalic secondary minerals may point to an alkalic fluid source, which experiments have shown can result in significant zircon alteration and dissolution-reprecipitation processes at moderate pressure, temperature, and pH conditions (e.g., Harlov and Dunkley, 2010).

Zircon crystals, particularly those from Pea Ridge sample PR-91, commonly have complex CL textures and discordant U-Pb systematics, providing further evidence for open system behavior and hydrothermal overprinting. Discordant Pea Ridge zircons have the highest REE, Fe, U, and Th, elements that are consistent with the geochemical enrichments found in the breccia pipes at Pea Ridge (cf. Ayuso et al., 2016, Fig. 11, Supplementary Data Table 5). Similar features have been documented in zircons from

granites coeval with the Olympic Dam IOCG deposit, in which higher Fe contents and xenotime overgrowths are attributed to metasomatic overprinting preceding mineralization (Courtney-Davies et al., 2019). Ti-in-zircon temperatures determined for PR-91 zircons were the lowest of any sample investigated, ~630–740 °C (Fig. 12). These temperatures are ~150–200 °C lower than those determined for the predominantly igneous zircons in Pea Ridge sample PR-12 (Fig. 12). They overlap thermometry results from Zr-in-rutile and Ti-in-quartz (~480–630 °C) determined for the same porphyry unit (2275) by (Hofstra et al., 2016), which those authors interpreted to reflect heating and recrystallization by hydrothermal fluids, followed by brecciation, decompression, and secondary precipitation.

Melt inclusions in sample PR-12 have REE concentrations and chondrite-normalized patterns that are identical to those determined for rhyolite whole-rocks at Pea Ridge and define a continuum with breccia pipes that have REE concentrations >100,000× chondrite values (Fig. 4). The striking similarity in REE patterns between the melt inclusions in the host rocks at Pea Ridge and the breccia pipes that represent one of the last phases of hydrothermal alteration in the composite IOA system, provide strong evidence that the REE were derived from the same or similar composition igneous intrusions, supporting a direct link between magmatism and mineralization. The enrichment in the breccia pipes by several orders of magnitude requires efficient scavenging and concentration of REE by fluids exsolved from underlying intrusions or leached from the solidified host rocks (see Section 5.4. on models of IOA and IOCG formation).

5.3. Geochronology constraints

Our new $^{207}Pb/^{206}Pb$ geochronology results indicate a zircon crystallization age of 1456 ± 9 Ma (concordia) or 1456 ± 12 Ma (weighted average) for Pea Ridge sample PR-12 (Fig. 10), which is younger than a weighted average age of 1474 ± 8 Ma published by Aleinikoff et al. (2016) for a zircon split of the same sample. Because our data are intentionally biased towards zircons with melt inclusions, the geochronology results are not necessarily expected to be equivalent. It may be that the melt inclusion-bearing zircons are skewed towards later stages of magmatism in the composite zircon record retained in the rock. Age data presented by Aleinikoff et al. (2016) and Neymark et al. (2016) for monazite, xenotime, and apatite from the breccia pipes and the amphibole-quartz and magnetite ore zones of the Pea Ridge deposit indicate that it was a long-lived system with numerous superimposed metasomatic events from ~1470 to 1440 Ma. An important new result of our study is that we now have direct evidence that magmatic activity at Pea Ridge was concurrent with these later phases of metasomatism and mineralization based on crystallization ages of melt inclusion-bearing zircons (Fig. 10). Aleinikoff et al. (2016) proposed an average breccia pipe formation age of ~1465 Ma using the dominant monazite $^{207}Pb/^{206}Pb$ age population, but these authors also found a cluster of younger monazite grains with a $^{207}Pb/^{206}Pb$ weighted average age of 1455 ± 10 Ma, which they interpreted to be a

separate episode of monazite growth. This age is identical to our new geochronology results for PR-12, supporting the role of Pea Ridge magmatism in the later phases of brecciation/re-brecciation and REE enrichment along the margins of the Pea Ridge IOA deposit. In addition, the ~1465 Ma breccia pipe age is identical within error to the zircon crystallization age of 1467 ± 13 Ma (concordia) or 1462 ± 11 Ma (weighted average) that we determined for Pea Ridge sample PR-91 (Fig. 10), based on a smaller number of concordant grains in a largely discordant and disrupted zircon population. We note that disrupted zircon systematics in PR-91 may be related to the younger 1456 Ma event apparent by our new zircon age data for sample PR-12 and the monazite age data in Aleinikoff et al. (2016).

Another important aspect of our geochronology data that diverges from previous studies is the documentation of >1550 Ma inherited zircons in both the Pea Ridge and Bourbon magmatic centers (Fig. 10). While it has been proposed that the 1550 Ma basement isopleth that marks the eastern edge of the Laurentian craton lies ~20 km west of the Pea Ridge deposit (Fig. 1, Bickford et al., 2015), the presence of >1550 Ma zircons in Pea Ridge and Bourbon samples indicate that this basement boundary extends at least as far east as these centers, and possibly farther. The lack of >1550 Ma zircons in the Eminence magmatic center at the southern end of the St. Francois Mountains terrane is consistent with it being located east of the craton boundary (Figs. 1 and 10). In all magmatic centers investigated, there is a large spread in concordant $^{207}Pb/^{206}Pb$ zircon ages that support the presence of multiple age populations that span tens of Myr. Discrete pulses of magmatism are difficult to discern given the large errors on individual zircons that are tens of Myr (Fig. 10). The Bourbon center has the overall oldest zircons, with about half of the grains >1500 Ma (1499 ± 11 Ma concordia age, 1486 ± 16 Ma weighted average age, Fig. 10). Zircons from the two dated Eminence samples have $^{207}Pb/^{206}Pb$ crystallization ages that overlap those of the Pea Ridge center (1452 ± 14 Ma and 1460 ± 10 Ma concordia ages, 1469 ± 17 Ma and 1458 ± 15 Ma weighted average ages, Fig. 10). The combined data indicate that silicic magmatism overlapped across broad temporal and spatial scales in the St. Francois Mountains terrane, including regions that produced IOA and IOCG mineralization and those that did not (Fig. 1).

5.4. Models of IOA and IOCG formation

Derivation of ore fluids from magmas, meteoric waters, surficial brines, or a combination thereof remain uncertain in IOA and IOCG formation (cf. Barton, 2014). One end member is the entirely non-magmatic model, whereby magmas supply the heat to drive hydrothermal convection but none of the constituent elements. On the other hand, magmas may be the primary source of metals, fluids, and ligands. Several key observations for the Pea Ridge system can be used to parse these end member scenarios. First, the contemporaneity of magmatism and mineralization based on zircon crystallization ages of the host igneous rocks (Fig. 10) and monazite, xenotime, and apatite ages of

different parts of the composite IOA ore body (Aleinikoff et al., 2016; Neymark et al., 2016) provide direct evidence for a temporal link. Second, there is a clear correlation between the geochemical attributes of the IOA deposit and Pea Ridge melt and mineral inclusions, including the REE patterns of melt inclusions and breccia pipes (Fig. 4), the presence of monazite and xenotime that reflect a hydrothermal transition and match compositions of those in the IOA ore zones (Fig. 8) and higher Fe, U, and REE in discordant zircons that are consistent with the unique geochemical signature of the IOA-REE deposit (Fig. 11). Third, the very high Cl in the melt inclusions (Fig. 3) indicates that Pea Ridge magmas had an enhanced ability to transport Fe and REE as Cl-complexed ore metals (e.g., Williams-Jones et al., 2012). The combined evidence provides strong support for a magmatic-hydrothermal model in the formation of the Pea Ridge IOA deposit.

One magmatic model that has been proposed for IOA deposits is an immiscible Fe-oxide melt model (cf. Velasco et al., 2016; Tornos et al., 2016, 2017). Fresh magnetite and ilmenite inclusions in refractory zircon crystals indicate that Pea Ridge magmas were reduced to mildly oxidized (log fO_2 −0.8 to −1.84 ΔNNO). Experiments have shown that producing an immiscible Fe-P-rich melt with a conjugate Si-rich melt requires extremely oxidized conditions, log fO_2 + 3 ΔFMQ or higher (Hou et al., 2018; Mungall et al., 2018). Furthermore, the low-moderate F (<0.4 wt%) and P (<0.3 wt% P_2O_5) in compositionally diverse Pea Ridge melt inclusions are inconsistent with the generation of an immiscible Fe-P-rich melt from a parental magma with >1 wt% F and >1.5 wt% P_2O_5 (cf. Hou et al., 2018; Xie et al., 2019). New oxygen isotope data also bear directly on tests of this model. For an average $\delta^{18}O$ value of 6.9‰ and Ti-in-zircon temperature of 880 °C for Pea Ridge zircons (Figs. 12 and 13), the calculated equilibrium magma (melt) $\delta^{18}O$ value is 8.3‰, based on $\Delta_{melt-zircon} \approx 1.4$‰ (Trail et al., 2009). Reported magnetite $\delta^{18}O$ values for the Pea Ridge IOA ore body range from 1.0 to 7.0‰ (Childress et al., 2016; Johnson et al., 2016). The upper end of this range, interpreted to be igneous, is consistent with a high-temperature equilibrium $\delta^{18}O$ value of about 5.3‰ for magnetite, based on $\Delta^{18}O_{melt-magnetite} \approx 3.0$‰ at 880 °C (Zhao and Zheng, 2003). It is inconsistent with an immiscibility model, for which the maximum $\Delta^{18}O$ between conjugate Si-rich and Fe-rich melts would be <1.0‰ (Lester et al., 2013). This finding is more broadly supported by a global O isotope compilation for IOA systems (Troll et al., 2019).

Another potential magmatic model to consider in the genesis of the Pea Ridge IOA deposit is a magnetite flotation model, in which igneous magnetite is transported and concentrated by exsolved magmatic fluids to shallower crustal levels where hydraulic fracturing leads to precipitation of massive iron oxides (e.g., Knipping et al., 2015a, b; Simon et al., 2018; Ovalle et al., 2018; Knipping et al., 2019). Titanium contents of igneous magnetite in Pea Ridge zircons of ~15 wt% TiO_2 overlap the highest end of the TiO_2 range for what has been interpreted as a relict igneous generation in the Pea Ridge iron ore body (Fig. 9, Childress et al., 2016). However, measured Al_2O_3 (~1.3 wt%), MnO

(~0.4 wt%) and V_2O_3 (~0.3 wt%) contents in the zircon-hosted magnetite inclusions are much higher than those of the interpreted relict igneous generation in Childress et al. (2016), which have <0.06 wt% Al_2O_3, <0.05 wt% MnO and <0.07 wt% V_2O_3. Magnetite inclusions in Pea Ridge zircons have Ti + V of ~9 wt% and Al + Mn of ~0.7 wt%, which is significantly higher than what have been interpreted as relict igneous magnetite populations at Pea Ridge and other IOA localities globally (e.g., Simon et al., 2018). High Ti in magnetite from different ore zones of the Pea Ridge IOA deposit have been attributed to mobility of Ti in magmatic-hydrothermal fluids that crystallize rutile (Hofstra et al., 2016). The current dataset does not support or require an igneous microlite model. The high Cl (~2000–5000 ppm) in Pea Ridge melt inclusions indicate that an exsolved magmatic fluid could transport Fe, without the requirement of magnetite wetting from a silicate melt, though it may have occurred as an incidental process (e.g., Hu et al., 2019).

The Cl contents of the Pea Ridge melt inclusions fall between the experimentally determined Cl-H_2O solubility curves for rhyolite and latite silicate melts saturated in vapor or hydrosaline liquid at 2 kbar (Webster, 2004). Decompression of silicate magmas as they were transported to shallower crustal levels would have promoted exsolution of hydrosaline fluids. Our data are consistent with this process happening in discrete pulses over tens of Myr as fresh melts of metasomatized mantle material supplied Cl to the overlying silicic magmas and/or solidified rocks, with volatile exsolution and gas sparging that stripped magmas and rocks of Fe, REE, and other constituent elements to generate the IOA ore body and REE-rich breccia pipes. Exsolved fluids may have been focused into cupolas above the crystallizing magma chambers (e.g., Lowenstern, 1994), released in episodic fracturing and brecciation of overlying rocks, and degassed during volcanic eruptions that formed ash-flow tuffs. A shallow marine basin or caldera lake at Pea Ridge (e.g., Hofstra et al., 2016) may have trapped some of the degassed Cl and other volatiles. Apatite from different ore zones of the Pea Ridge IOA deposit have geochemical signatures consistent with magmatic and basinal brine components (Mercer et al., 2020). Experimental studies show that solubility of Cl in silicate melts decreases with increasing degree of evolution of the melt, with the strongest contribution of Cl from the more mafic progenitor magmas (e.g., Aiuppa et al., 2009). Bourbon and Pea Ridge trachydacite melts may have evolved from or coexisted with mafic to intermediate magmas based on their high liquidus temperatures and pressures, high zircon crystallization temperatures, and zircon isotopic ranges that encompasses mantle to near-mantle $\delta^{18}O$ values (Figs. 6, 12 and 13).

5.5. Crustal pathways of mineralization

Zircons from drill core intercepts of the Granite-Rhyolite province provide a unique opportunity to probe the crustal architecture in relation to IOA and IOCG mineralization in southeast Missouri. Geochronology data show that a cratonic crustal boundary defined by the 1550 Ma isopleth extends at least 20 km farther east than

is currently mapped to encompass the Pea Ridge and Bourbon magmatic centers, which have inherited zircons that span from 1550 to 1618 Ma (Fig. 1, see 4.3 Zircon geochronology, 5.3 Geochronology constraints). The 3D expression of the boundary between cratonic basement and accreted continental crust is not known, but depth-integrated magnetic susceptibility and density maps indicate that it is not a sharp orthogonal contact (McCafferty et al., 2019). In plan view, its northeast to southwest orientation is perpendicular to a ~100 km wide northwest to southeast trending belt defined by low gravity (Missouri Gravity Low) and high electrical conductivity (Missouri High Conductivity Belt) (Fig. 14, DeLucia et al., 2019). Overlapping these geophysical anomalies is a ~50 km wide by ~200 km long northwest to southeast crustal corridor of high magnetic susceptibility (Fig. 14, McCafferty et al., 2019). The Pea Ridge and Bourbon centers lie near the intersection of these collocated geophysical anomalies, whereas the Eminence center is separated ~110 km to the south (Fig. 14). IOA mineralization at Pea Ridge and Bourbon and the lack of mineralization at Eminence indicate that their disparate crustal settings may account for differences in mineralization potential.

In addition to new lines of evidence from geochronological data, Pea Ridge and Bourbon zircons have unique geochemical signatures relative to Eminence zircons that provide important new insights into their different crustal settings. Pea Ridge and Bourbon zircons have $\delta^{18}O$ values of 5.5–7.9‰, which overlap published zircon data from the Butler Hill and Taum Sauk calderas located ~80 km southeast in the St. Francois Mountains terrane (Figs. 1,

13, 14, King et al., 2008). These values span from mantle to crustal, whereas zircons from the Eminence center have very high-$\delta^{18}O$ values of 8.3–9.6‰ that are distinctly supracrustal and require sedimentary components in their genesis (Fig. 13, e.g., Watts et al., 2016, 2019). A connection between magmatic sources of the Pea Ridge, Bourbon, Butler Hill, and Taum Sauk calderas is supported by the ~200 km long high magnetic susceptibility corridor, interpreted to represent a linked magmatic plumbing system of the southeast Missouri iron mineral system (Fig. 14, McCafferty et al., 2019). Trace element abundances in Pea Ridge melt inclusions span the within-plate granite to volcanic arc granite fields, consistent with their derivation from cratonic and volcanic arc sources, whereas Eminence melt inclusions span the volcanic arc and syncollisional granite fields, consistent with their derivation from both arc and sedimentary (perhaps collisionally thickened?) crustal sources (Fig. 5). Eminence melt inclusions have higher water contents, lower temperatures, and lower pressures relative to Pea Ridge and Bourbon melt inclusions (Fig. 6). Pea Ridge and Bourbon melt inclusions extend to less-evolved trachydacite compositions with very high Cl contents (Fig. 3) that correlate with lower silica and higher total alkalis (Fig. 2). The combined evidence indicates that Pea Ridge and Bourbon magmas were derived from deeper melts of metasomatized mantle and cratonic crust along a boundary defined by geochronological, isotopic, and geophysical datasets. Decompression melting in either a back-arc setting or rifted section of a volcanic arc located above a previously metasomatized mantle source is consistent with our data. Whereas Pea Ridge
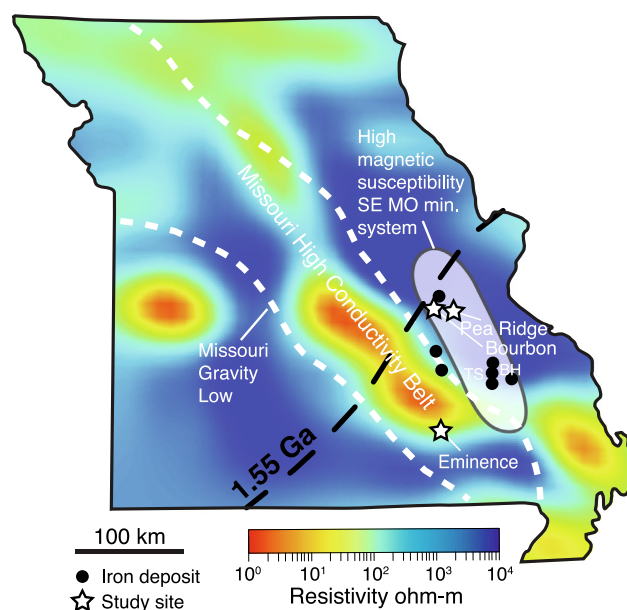

Fig. 14. Map of Missouri showing relevant geophysical features (adapted from McCafferty et al., 2019; DeLucia et al., 2019). The colored base map shows a resistivity model of magnetotelluric data for a 35 km depth slice, with the Missouri High Conductivity Belt labeled. Overlain on this base map are the boundaries of the Missouri Gravity Low (bold dashed white lines), the high magnetic susceptibility corridor of the southeast Missouri iron mineral system (shaded white area), and the 1.55 Ga isopleth (bold dashed black line). The locations of iron deposits and the study sites for this work are shown by the symbols, and the approximate locations of the Butler Hill (BH) and Taum Sauk (TS) calderas are labeled.

and Bourbon magmas were relatively hot and dry, Eminence magmas formed during cool and wet arc melting processes in the shallow crust, with assimilation of sedimentary material.

Lithologic contrasts between the cratonic crustal block and accreted terranes may have been favorable for focusing silicic magmatism in the St. Francois Mountains terrane. Transtensional tectonics in southeast Missouri during the Mesoproterozoic would have facilitated dilation of the crust, creating space for felsic melts and opening conduits for mineralizing fluids (e.g., Lowell et al., 2010; DeLucia et al., 2019). Pea Ridge and Bourbon, which exist at the intersection of the 1550 Ma isopleth with boundaries of crustal domain(s) defined by gravity, magnetic, and magnetotelluric data (Fig. 14), would have been located in a zone of exceptional crustal weakness with dense fault networks. These zones of weakness may have been exploited repeatedly over tens of Myr as pulsed magmatism evolved along the Laurentian margin. A magmatic-hydrothermal model, whereby ore fluids and metals were derived from Pea Ridge and Bourbon magmas is consistent with our data. Our data indicate that trachydacite to low-silica rhyolite melt inclusions with high Cl are the most promising sources of ore fluids. This model is bolstered by previously published results that show (1) Nd and Pb isotopic data linking magnetite ore, REE breccias, rhyolite host rocks, and regional mafic to intermediate rocks (Ayuso et al., 2016), (2) O isotopic data for magnetite and S isotopic data for sulfides that indicate a magmatic fluid component in Pea Ridge ore zones (Johnson et al., 2016; Childress et al., 2016), (3) geochemical attributes of fluid inclusions in mineral alteration zones that can be linked to a magmatic source, such as Fe, Mg, and Ca that point to a mafic to intermediate magmatic source (Hofstra et al., 2016), and (4) geochemical data for apatite in IOA ore zones that support crystallization from a Cl-rich magmatic-hydrothermal fluid (Mercer et al., 2020).

6. CONCLUSIONS

Melt inclusions hosted in refractory zircon crystals have enabled the first direct analyses of Mesoproterozoic silicic magmatic systems in the St. Francois Mountains terrane. Combining high-spatial resolution melt and mineral inclusion data with zircon geochronology, geochemistry, and isotope geochemistry, this study provides robust evidence for a linked magmatic-hydrothermal origin of the Pea Ridge IOA-REE deposit. Our data are consistent with magmatism in a back-arc or rifted segment of a volcanic arc in which melting of metasomatized mantle components imparted Pea Ridge magmas with distinctive geochemical features, such as their alkalinity and high Cl contents, which enabled them to transport and concentrate Fe and REE in the shallow crust. The primary magmas did not have initially high concentrations of Fe, REE, or other elements associated with IOA and IOCG deposits. Geochronological and geochemical evidence for cratonic crustal contributions underscore the importance of the local crustal architecture beneath the Pea Ridge system, in which lithosphere-scale zones of weakness focused silicic magmas

and facilitated fluid flow in the upper crust. Zircon textures and geochemistry indicate that host rocks of the Pea Ridge IOA-REE deposit contain a composite record of tens of Myr of magmatism and mineralization. Our new results support a model wherein underlying magmas repeatedly fluxed the overlying rocks with volatiles that led to hydrothermal replacement of rhyolite host rocks, with massive iron oxide deposition and formation of REE-rich breccia pipes. Based on distinctive geochemical similarities with the Pea Ridge deposit, the Bourbon locality may be promising for future exploration efforts to identify additional REE resources in the St. Francois Mountains terrane. Finally, this study demonstrates the utility of a new zircon-scale approach to deciphering the complex magmatic histories inherent in IOA and IOCG deposits. Growing societal demand for metals and critical REE will require such innovative methods to understand their global occurrences and ensure future supplies.

APPENDIX A. SUPPLEMENTARY MATERIAL

Supplementary data to this article can be found online at https://doi.org/10.1016/j.gca.2019.12.032 and in the Watts and Mercer (2020) U.S. Geological Survey data release at https://doi.org/10.5066/P9TFVXR5.

REFERENCES

Aiuppa A., Baker D. and Webster J. (2009) Halogens in volcanic systems. *Chem. Geol.* **263**, 1–18.

Aleinikoff J. N., Selby D., Slack J. F., Day W. C., Pillers R. M., Cosca M. A., Seeger C. M., Fanning C. M. and Samson I. M. (2016) U-Pb, Re-Os, and Ar/Ar geochronology of rare earth element (REE)-rich breccia pipes and associated host rocks from the Mesoproterozoic Pea Ridge Fe-REE-Au deposit, S. Francois Mountains, Missouri. *Econ. Geol.* **111**, 1883–1914.

Ayuso R. A., Slack J. F., Day W. C. and McCafferty A. E. (2016) Geochemistry, Nd-Pb isotopes, and Pb-Pb ages of Mesoproterozoic Pea Ridge iron oxide-apatite-rare earth element deposit, southeast Missouri. *Econ. Geol.* **111**, 1935–1962.

Barra F., Reich M., Selby D., Rojas P., Simon A., Salazar E. and Palma G. (2017) Unraveling the origin of the Andean IOCG clan: A Re-Os isotope approach. *Ore Geol. Rev.* **81**, 62–78.

Barth A. P. and Wooden J. L. (2010) Coupled elemental and isotopic analyses of polygenetic zircons from granitic rocks by ion microprobe, with implications for melt evolution and the sources of granitic magmas. *Chem. Geol.* **277**, 149–159.

Barton M. D. (2014) Iron oxide (-Cu-Au-REE-P-Ag-U-Co) systems. In Treatise on Geochemistry 2nd ed. 13, pp. 515–541.

Bickford M. E., Van Schmus W. R., Karlstrom K. E., Mueller P. A. and Kamenov G. D. (2015) Mesoproterozoic-trans-Laurentian magmatism: A synthesis of continent-wide age distributions, new SIMS U-Pb ages, zircon saturation temperatures, and Hf and Nd isotopic compositions. *Precam. Res.* **265**, 286–312.

Bindeman I. N., Schmitt A. K., Lundstrum C. C. and Hervig R. L. (2018) Stability of zircon and its isotopic ratios in high-temperature fluids: long-term (4 months) isotope exchange experiment at 850 C and 50 MPa. *Front. Ear. Sci.* **6**, 59.

Black L. P., Kamo S. L., Allen C. M., Davis D. W., Aleinikoff J. N., Valley J. W., Mundil R., Campbell I. H., Korsch R. J., Williams I. S. and Foudoulis C. (2004) Improved $^{206}Pb/^{238}U$ microprobe geochronology by the monitoring of a trace-element–related matrix effect; SHRIMP, ID-TIMS, ELA-ICP-MS and oxygen isotope documentation for a series of zircon standards. *Chem. Geol.* **205**, 115–140.

Childress T. M., Simon A. C., Day W. C., Lundstrom C. C. and Bindeman I. N. (2016) Iron and oxygen isotope signatures of the Pea Ridge and Pilot Knob magnetite-apatite deposits, southeast Missouri, USA. *Econ. Geol.* **111**, 2033–2044.

Courtney-Davies L., Ciobanu D. L., Verdugo-Ihl M. R., Slattery A., Cook N. J., Dmitrijeva M., Keyser W., Wade B. P., Domnick U. I., Ehrig K., Xu J. and Kontonikas-Charos A. (2019) Zircon at the nanoscale records metasomatic processes leading to large magmatic-hydrothermal ore systems. *Minerals* **9**, 364.

Cullison J. S. and Ellison S. P. (1944) Diamond drill core from Bourbon high, Crawford County, Missouri. *J. Geol.* **28**, 1386–1396.

Damon P. E. (1949) Radioactivity and mineralization in a rhyolite porphyry. *Univ. Ark. Inst. Sci. Tech.*, 94–101.

Dare S. A., Barnes S.-J. and Beaudoin G. (2015) Did the massive magnetite "lava flows" of El Laco (Chile) form by magmatic or hydrothermal processes? New constraints from magnetite composition by LA-ICP-MS. *Mineral. Depos.* **50**, 607–617.

Day W. C., Seeger C. M. and Rye R. O. (2001) Review of the iron oxide deposits of Missouri—magmatic end members of the iron oxide-Cu-Au-U-REE deposit family. *Geol. Soc. Am. Abs. w. Prog.* **33**(6), 4.

Day W. C., Slack J. F., Ayuso R. A. and Seeger C. M. (2016) Regional geologic and petrologic framework for iron oxide ± apatite ± rare earth element and iron oxide copper-gold deposits of the Mesoproterozoic St. Francois Mountains terrane, southeast Missouri, USA. *Econ. Geol.* **111**, 1825–1858.

DeLucia M. S., Murphy B. S., Marshak S. and Egbert G. D. (2019) The Missouri High-Conductivity Belt, revealed by magnetotelluric imaging: evidence of a trans-lithospheric shear zone beneath the Ozark Plateau, Midcontinent, USA? *Tectonophys.* **753**, 111–123.

du Bray E. A., Day W. C. and Meighan C. J. (2018) Compilation of new and previously published geochemical and modal data for Mesoproterozoic igneous rocks of the St. Francois Mountains, southeast Missouri. *USGS Dat. Ser.* **1080**, 10 p.

Ferry J. M. and Watson E. B. (2007) New thermodynamic models and revised calibrations for the Ti-in-zircon and Zr-in-rutile thermometers. *Contrib. Mineral. Petrol.* **154**, 429–437.

Geisler T., Schaltegger U. and Tomaschek F. (2007) Re-equilibration of zircon in aqueous fluids and melts. *Elements* **3**, 43–50.

Ghiorso M. S. and Evans B. W. (2008) Thermodynamics of rhombohedral oxide solid solutions and a revision of the Fe–Ti two-oxide geothermometer and oxygen-barometer. *Am. Jour. Sci.* **308**, 957–1039.

Groves D. I. P., Bierlein F. P., Meinert L. D. and Hitzman M. W. (2010) Iron oxide copper–gold (IOCG) deposits through Earth history; implications for origin, lithospheric setting, and distinction from other epigenetic iron oxide deposits. *Econ. Geol.* **105**, 641–654.

Gualda G. A., Ghiorso M. S., Lemons R. V. and Carley T. L. (2012) Rhyolite-MELTS: a modified calibration of MELTS optimized for silica-rich, fluid-bearing magmatic systems. *J. Petrol.* **53**, 875–890.

Harlov D. E. and Dunkley D. (2010) Experimental high-grade alteration of zircon using alkali- and Ca-bearing solutions: resetting the zircon geochronometer during metasomatism. *Am. Geophys. Un. Abs.*, V41D-2301.

Johnson C. A., Day W. C. and Rye R. O. (2016) Oxygen, hydrogen, sulfur, and carbon isotopes in the Pea Ridge magnetite-apatite deposit, southeast Missouri, and sulfur isotope comparisons to other iron deposits in the region. *Econ. Geol.* **111**, 2017–2032.

Harlov D. E., Meighan C. J., Kerr I. D. and Samson I. M. (2016) Mineralogy, chemistry, and fluid-aided evolution of the Pea Ridge Fe oxide-(Y+REE) deposit, southeast Missouri, USA. *Econ. Geol.* **111**, 1963–1984.

Harrison R. W., Lowell G. R. and Unruh D. M. (2000) Geology, geochemistry, and age of Mesoproterozoic igneous rocks in the Eminence-Van Buren area: A major structural outlier of the St. Francois terrane, south-central Missouri. *Geol. Soc. Am. Abs. w. Prog.* **32**(3), A-14.

Harrison R. W., Orndorff R. C. and Weary D. J. (2002) Geology of the Stegall Mountain 7.5-minute quadrangle, Shannon and Carter Counties, south-central Missouri. *USGS Geol. Inves. Ser.*, Map I-2767, scale 1:24,000.

Hervig R. L., Mazdab F. K., Williams P., Guan Y., Huss G. P. and Leshin L. A. (2006) Useful ion yields for Cameca IMS 3f and 6f SIMS: limits on quantitative analysis. *Chem. Geol.* **227**, 83–99.

Hitzman M. W., Oreskes N. and Einaudi M. T. (1992) Geological characteristics and tectonic setting of Proterozoic iron oxide (Cu–U–Au–REE) deposits. *Precam. Res.* **58**, 241–287.

Hofstra A. H., Meighan C. J., Song X., Samson I., Marsh E. E., Lowers H. A., Emsbo P. and Hunt A. G. (2016) Mineral thermometry and fluid inclusion studies of the Pea Ridge iron oxide-apatite–rare earth element deposit, Mesoproterozoic St. Francois Mountains terrane, southeast. *Econ. Geol.* **111**, 1985–2016.

Hou T., Charlier B., Holtz F., Veksler I., Zhang Z., Thomas R. and Namur O. (2018) Immiscible hydrous Fe-Ca-P melt and the origin of iron oxide-apatite ore deposits. *Nat. Comm.* **9**, 1415.

Hu H., Li J. -W., Harlov D. E., Lentz D. R., McFarlane and C.R. M. (2019) A genetic link between iron oxide-apatite and iron skarn mineralization in the Jinniu volcanic basin, Daye district, eastern China: evidence from magnetite geochemistry and multi-mineral U-Pb geochronology. Geol. Soc. Am. Bull

Ireland T. R. and Williams I. S. (2003) Considerations in zircon geochronology by SIMS. *Rev. Mineral. Geochem.* **53**, 215–241.

King E. M., Trzaskus A. P. and Valley J. W. (2008) Oxygen isotope evidence for magmatic variability and multiple alteration events

in the Proterozoic St. Francois Mountains, Missouri. *Precam. Res.* **165**, 49–60.

Kisvarsanyi G. and Proctor P. D. (1967) Trace element content of magnetites and hematites, southeast Missouri metallogenic province, U.S.A. *Econ. Geol.* **62**, 449–471.

Kisvarsanyi E. B. (1981) Geology of the Precambrian St. Francois terrane, southeastern Missouri. Miss. Dept. Nat. Res.. *Contrib. Precam. Geol. 8, Rep. Inves.* **64**, 58.

Kita N. T., Ushikubo T., Fu B. and Valley J. W. (2009) High precision SIMS oxygen isotope analyses and the effect of sample topography. *Chem. Geol.* **264**, 43–57.

Knipping J. L., Bilenker L., Simon A. C., Reich M., Barra F., Deditius A., Lundstrom C., Bindeman I. and Munizaga R. (2015a) Giant Kiruna-type deposits form by efficient flotation of magmatic magnetite suspensions. *Geol.* **43**, 591–594.

Knipping J. L., Bilenker L., Simon A. C., Reich M., Barra F., Deditius A., Wälle M., Heinrich C. A., Holtz F. and Munizaga R. (2015b) Trace elements in magnetite from massive iron oxide-apatite deposits indicate a combined formation by igneous and magmatic-hydrothermal processes. *Geochim. Cosmochim. Acta* **171**, 15–38.

Knipping J. L., Webster J. D., Simon A. C. and Holtz F. (2019) Accumulation of magnetite by flotation on bubbles during decompression of silicate magma. *Sci. Rep.* **9**, 3852.

Lester G. W., Kyser T. K. and Clark A. H. (2013) Oxygen isotope partitioning between immiscible silicate melts with H2O, P and S. *Geochim. Cosmochim. Acta* **109**, 306–311.

Ludwig K. R. (2009) SQUID 2: A User's Manual. Berkeley Geochron. Cent. Spec. Pub. 5.

Ludwig K. R. (2012) Isoplot 3.75, a geochronological toolkit for Excel. Berkeley Geochron. Cent. Spec. Pub. 5.

Lowell G. R., Harrison R. W., Weary D. J., Orndorff R. C., Repetski J. E. and Pierce H., (2010) Rift-related volcanism and karst geohydrology of the southern Ozark dome. Precambrian Rift Volcanoes to the Mississippian Shelf Margin: Geological Field Excursions in the Ozark Mountains (eds. K.R. Evans and J.S. Aber). Geol. Soc. Am. Field Guide 17, 99–158.

Lowenstern J. (1994) Dissolved volatile concentrations in an ore-forming magma. *Geology* **22**, 893–896.

Macdonald R., Smith R. L. and Thomas J. E. (1992) Chemistry of the subalkalic silicic obsidians. USGS Prof. Pap. 152.

McCafferty A. E., Phillips J. D. and Driscoll R. L. (2016) Magnetic and gravity gradiometry framework for Mesoproterozoic iron oxide-apatite and iron oxide-copper-gold deposits, southeast Missouri. *Econ. Geol.* **111**, 1859–1882.

McCafferty Anne E., Phillips Jeffrey D., Hofstra Albert H. and Day Warren C. (2019) Crustal architecture beneath the southern Midcontinent (USA) and controls on Mesoproterozoic iron-oxide mineralization from 3D geophysical models. *Ore Geol. Rev.* **111**, 102966. https://doi.org/10.1016/j.oregeorev.2019.102966.

McDonough W. F. and Sun S. (1995) The composition of the Earth. *Chem. Geol.* **120**, 223–253.

McMillan W. D. (1946) Exploration of the Bourbon magnetic anomaly, Crawford County, Missouri. US Bur. of Mines, Rep. of Inves. 3961, October, 1946.

Meert J. G. and Santosh M. (2017) The Columbia supercontinent revisited. *Gond. Res.* **50**, 67–83.

Menuge J. F., Brewer T. S. and Seeger C. M. (2002) Petrogenesis of metaluminous A-type rhyolites from the St. Francois Mountains, Missouri and the Mesoproterozoic evolution of the southern Laurentian margin. *Precam. Res.* **113**, 269–291.

Mercer C. N., Hofstra A. H., Todorov T. I., Roberge J., Burgisser A., Adams D. T. and Cosca M. (2015) Pre-eruptive conditions of the Hideaway Park topaz rhyolite: insights into metal source

and evolution of magma parental to the Henderson porphyry molybdenum deposit, Colorado. *J. Petrol.* **56**, 645–679.

Mercer C. N., Watts K. E. and Gross J. (2020) Apatite trace element geochemistry and cathodoluminescent textures – A comparison between regional magmatism at Pea Ridge IOA-REE and Boss IOCG deposits, southeastern Missouri iron metallogenic province, USA. *Ore Geol. Rev.* **116** 103129.

Mungall J. E., Long K., Brennan J. M., Smythe D. and Naslund H. R. (2018) Immiscible shoshonitic and Fe-P-oxide melts preserved in unconsolidated tephra at El Laco volcano. *Chile. Geol.* **46**, 255–258.

Neymark L. A., Holm-Denoma C. S., Pietruszka A. J., Aleinikoff J. N., Fanning C. M., Pillers R. M. and Moscati R. J. (2016) High spatial resolution U-Pb geochronology and Pb isotope geochemistry of magnetite-apatite ore from the Pea Ridge iron oxide-apatite deposit, St. Francois Mountains, southeast Missouri, USA. *Econ. Geol.* **111**, 1915–1933.

Nold J. L., Dudley M. A. and Davidson P. (2014) The southeast Missouri (USA) Proterozoic iron metallogenic province—types of deposits and genetic relationships to magnetite-apatite and iron oxide-copper-gold deposits. *Ore Geol. Rev.* **57**, 154–171.

Nuelle L. M., Day W. C., Sidder G. B. and Seeger C. M. (1992) Geology and mineral paragenesis of the Pea Ridge iron ore mine, Washington County, Missouri—origin of the rare-earth-element- and gold-bearing breccia pipes. *USGS Bull.* **1989**, A1–A11.

Oreskes N. and Einaudi M. T. (1990) Origin of REE-enriched hematite breccias at the Olympic Dam Cu–U–Au–Ag deposit, Roxby Downs, South Australia. *Econ. Geol.* **85**, 1–28.

Orndorff R. C., Harrison R. W. and Weary D. J. (1999) Geologic map of the Eminence quadrangle, Shannon County, Missouri. USGS Geol. Invest. Ser. Map I-2653, scale 1:24,000

Ovalle J. T., La Cruz N. L., Reich M., Barra F., Simon A. C., Konecke B., Rodriquez-Mustafa M. A., Deditius A. P., Childress T. M. and Morato D. (2018) Formation of massive iron deposits linked to explosive volcanic eruptions. *Sci. Rep.* **8**, 14855.

Pearce J. A., Harris B. W. and Tindle A. G. (1984) Trace element discrimination diagrams for the tectonic interpretation of granitic rocks. *J. Petrol.* **25**, 956–983.

Pratt W. P., Anderson R. E., Berry A. W., Bickford M. E., Kisvarsanyi E. B. and Sides J. R. (1979) Geologic map of exposed Precambrian rocks, Rolla 1 degree by 2 degrees quadrangle, Missouri. USGS Geol. Invest. Ser. Map I-1161, scale 1:250,000.

Seeger C. M. (2000) Southeast Missouri iron metallogenic province: Characteristics and general chemistry. In *Hydrothermal iron oxide copper-gold and related deposits: A global perspective*, 1 (ed. T. M. Porter). PGC Publishing, Adelaide, Australia, pp. 237–248.

Seeger C. M. (2003) *Lithology and alteration assemblages of the Boss iron-copper deposit, Iron and Dent Counties, southeast Missouri* Ph.D. thesis. Univ. of Missouri-Rolla, p. 139.

Seeger C. M., Nuelle L. M., Day W. C., Sidder G. B., Marikos M. A. and Smith D. C. (2001) Geologic maps and cross sections of mine levels at the Pea Ridge iron mine, Washington County, Missouri. USGS Misc. Field Map MF-2353, scale 1:2,400, 5 sheets, 6 p.

Sillitoe R. H. (2003) Iron oxide–copper–gold deposits: an Andean view. *Mineral. Depos.* **38**, 787–812.

Simon A. C., Knipping J. L., Reich M., Barra F., Deditius A., Bilenker L. and Childress T. (2018) Kiruna-type iron oxide-apatite (IOA) and iron oxide copper-gold (IOCG) deposits form by a combination of igneous and magmatic-hydrothermal processes: evidence from the Chilean iron belt. *Soc. Econ. Geol. Spec. Pub.* **21**, 89–114.

Slack J. F., Corriveau L. and Hitzman M. W. (2016) A special issue devoted to Proterozoic iron oxide-apatite (± REE) and iron oxide copper-gold and affiliated deposits of the southeast Missouri, USA, and the Great Bear magmatic zone, Northwest Territories, Canada: Preface. *Econ. Geol.* **111**, 1803–1814.

Stacey J. S. and Kramers J. D. (1975) Approximation of terrestrial lead isotope evolution by a two-stage model. *Earth Planet. Sci. Lett.* **26**, 207–221.

Tappert M. C., Rivard B., Giles D., Tappert R. and Mauger A. (2013) The mineral chemistry, near-infrared, and mid-infrared reflectance spectroscopy of phengite from the Olympic Dam IOCG deposit, South Australia. *Ore Geol. Rev.* **53**, 26–38.

Tornos F., Velasco F. and Hanchar J. M. (2016) Iron oxide melts, magmatic magnetite, and superheated magmatic-hydrothermal systems: The El Laco deposit, Chile. *Geol.* **44**, 427–430.

Tornos F., Velasco F. and Hanchar J. M. (2017) The magmatic to magmatic-hydrothermal evolution of the El Laco Depsoit (Chile) and its implications for the genesis of magnetite-apatite deposits. *Econ. Geol.* **112**, 1595–1628.

Trail D., Bindeman I. N., Watson E. B. and Schmitt A. K. (2009) Experimental calibration of oxygen isotope fractionation between quartz and zircon. *Geochim. Cosmochim. Acta* **73**, 7110–7126.

Troll V. R., Weis F. A., Jonsson E., Andersson U. B., Majidi S. A., Hogdahl K., Harris C., Millet M.-A., Chinnasamy S. S., Kooijman E. and Nilsson K. P. (2019) Global Fe-O isotope correlation reveals magmatic origin of Kiruna-type apatite-iron-oxide ores. *Nat. Comm.* **10**, 1712.

Valley J. W. (2003) Oxygen isotopes in zircon. In Zircon: Review in Mineralogy and Geochemistry (eds. J.M. Hanchar and P.W. O. Hoskin) 53, pp. 343–385.

Valley J. W., Kinny P. D., Schulze D. J. and Spicuzza M. J. (1998) Zircon Megacrysts from Kimberlite: oxygen Isotope Variability Among Mantle Melts. *Contrib. Mineral. Petrol.* **133**, 1–11.

Valley J. W., Lackey J. S., Cavosie A. J., Clechenko C. C., Spicuzza M. J., Basei M. A. S., Bindeman I. N., Ferreira V. P., Sial A. N., King E. M., Peck W. H., Sinha A. K. and Wei C. S. (2005) 4.4 billion years of crustal maturation: oxygen isotope ratios of magmatic zircons. *Contrib. Mineral. Petrol.* **150**, 561–580.

Van Schmus W. R., Bickford M. E. and Turek A. (1996) Proterozoic geology of the east-central Midcontinent basement. *Geol. Soc. Am. Spec. Pap.* **308**, 7–31.

Velasco F., Tornos F. and Hanchar J. M. (2016) Immiscible iron- and silica-rich melts and magnetite geochemistry at the El Laco volcano (northern Chile): evidence for a magmatic origin for the magnetite deposits. *Ore Geol. Rev.* **79**, 346–366.

Verplanck P. L. and Hitzman M. W., eds. (2016) Rare earths and critical elements in ore deposits. Rev. Econ. Geol. 18, p. 372.

Watts K. E. and Mercer C. N. (2020) Geochemistry, geochronology, and isotope geochemistry data for zircons and zircon-hosted melt and mineral inclusions in the St. Francois Mountains terrane, Missouri, U.S. Geological Survey data release, https://doi.org/10.5066/P9TFVXR5.

Watts K. E., John D. A., Colgan J. P., Henry C. D., Bindeman I. N. and Schmitt A. K. (2016) Probing the volcanic-plutonic connection and the genesis of crystal-rich rhyolite in a deeply dissected supervolcano in the Nevada Great Basin: Source of the late Eocene Caetano Tuff. *J. Petrol.* **57**, 1599–1644.

Watts K. E., John D. A., Colgan J. P., Henry C. D., Bindeman I. N. and Valley J. W. (2019) Oxygen isotopic investigation of silicic magmatism in the Stillwater caldera complex, Nevada: Generation of large-volume, low-δ^{18}O rhyolitic tuffs and assessment of their regional context in the Great Basin of the western United States. *Geol. Soc. Am. Bull.* **131**, 1133–1156.

Webster J. D. (2004) The exsolution of magmatic hydrosaline chloride liquids. *Chem. Geol.* **210**, 33–48.

Whitmeyer S. J. and Karlstrom K. E. (2007) Tectonic model for the Proterozoic growth of North America. *Geosph.* **3**, 220–259.

Wilke S., Holtz F., Neave D. A. and Almeev R. (2017) The effect of anorthite content and water on quartz-feldspar cotectic compositions in the rhyolitic system and implications for geobarometry. *J. Petrol.* **58**, 789–818.

Williams I. S. (1997) U-Th-Pb geochronology by ion microprobe: not just ages but histories. *Soc. Econ. Geol. Rev. Econ. Geol.* **7**, 1–35.

Williams P. J., Barton M. D., Johnson D. A., Fontbote L., De Haller A., Geordie M., Oliver N. H. S. and Marschik R. (2005) Iron-oxide–copper–gold deposits: geology, space–time distribution, and possible modes of origin. *Econ. Geol. 100th Ann. Vol.*, 371–406.

Williams-Jones A. E., Migdisov A. A. and Samson I. M. (2012) Hydrothermal mobilization of the rare earth elements: a tale of "ceria" and "yttria". *Elem.* **8**, 355–360.

Wright H. M., Bacon C. B., Vazquez J. A. and Sisson T. W. (2012) Sixty thousand years of magmatic volatile history before the caldera-forming eruption of Mount Mazama, Crater Lake, Oregon. *Contrib. Mineral. Petrol.* **164**, 1027–1052.

Xie Q., Zhang Z., Hou T., Cheng Z., Campos E., Wang Z. and Fei X. (2019) New insights for the formation of Kiruna-type iron deposits by immiscible hydrous Fe-P melt and high-temperature hydrothermal processes: evidence from El Laco Deposit. *Econ. Geol.* **114**, 35–46.

Zhao Z.-F. and Zheng Y.-F. (2003) Calculation of oxygen isotope fractionation in magmatic rocks. *Chem. Geol.* **193**, 59–80.

Associate Editor: Edward M. Ripley